Image Registration for Automated Alignment and Ordering of Non-neoplastic Kidney Biopsy Sections

Jennifer Janani Antonythasan

Acknowledgements

I would like to express my gratitude to my supervisors, Sabine Leh and Hrafn Weishaupt, for taking me on this project despite my limited programming knowledge. Their continuous guidance and support have been essential throughout this journey.

Sabine, your constant support, and positivity have been a big source of encouragement. Thank you for always motivating me and believing in my abilities. Hrafn, your patience and understanding, especially considering my limited programming background, have been invaluable. The progress I have made in the programming part of my thesis is largely due to your guidance. I am also grateful to everyone in the research group for their continuous support and for creating a positive and collaborative environment.

A special thank you to my mother, whose strength and support have been my backbone through both good and bad times. Your unconditional love and encouragement have been my greatest motivation. To my father, your constant blessings, even though you are no longer with us, continue to inspire me every day.

I also extend my thanks to all my friends and relatives for their support. A special mention goes to Shrutha Morthala, for joining me in working on my thesis during weekends, making it more enjoyable. And to Natalie Kavli, thank you for the ice cream breaks and for motivating when needed.

Thank you all for your invaluable support and encouragement.

Table of Contents

List of Figures

Følsomhet Intern (gul)

List of Tables

List of Abbreviations

Chronic Kidney Disease (CKD)

End-Stage Kidney Disease (ESKD)

Digital Pathology (DP)

Whole Slide Imaging (WSI)

Proximal convoluted tubule (PCT)

Distal convoluted tubule (DCT)

Tubulointerstitial nephritis (TIN)

Acute tubular injury (ATI)

Glomerular Filtration Rate (GFR)

Hematoxylin and Eosin (H&E)

Periodic acid-Schiff (PAS)

Artificial Intelligence (AI)

Machine Learning (ML)

Deep learning (DL)

Area Under the Curve (AUC)

Black and Tan BRachyury (BTBR)

Deep Feature Based Registration (DFBR)

Random-access memory (RAM)

Intersection Over Union (IOU)

Dice Score (DSC)

Abstract

The kidney, a vital organ responsible for waste excretion and hormone regulation, is frequently afflicted by non-neoplastic diseases affecting components like glomeruli and tubules. Chronic kidney disease (CKD), often progressing to end-stage kidney disease (ESKD), presents a substantial global health challenge. With nearly 100 million Europeans affected by CKD and projections indicating it may become a leading cause by 2040, there is an urgent need for advanced diagnostics, particularly in the under-researched area of non-neoplastic kidney diseases.

Digital pathology (DP) has transformed biomedical research and pathology diagnostics through the utilization of Whole Slide Images (WSIs) for precise tissue analysis. Image registration, a key application in DP, enables the alignment of histological sections, facilitating accurate comparisons and comprehensive tissue analysis. This thesis endeavours to integrate image registration tool into a future pipeline designed to automate the alignment and ordering of non-neoplastic kidney biopsy sections.

The thesis begins with a literature review to find image registration tools. Then the image registration tools found; HistokatFusion (commercial) and TIAToolbox (open source) were evaluated for a potential integration into a future pipeline aimed at automating the alignment and ordering of non-neoplastic kidney biopsy sections from Haukeland University Hospital, bergen. Through the application of Intersection Over Union (IOU) and Dice Score (DSC) metrics, the effectiveness of these tools is assessed, leading to the selection of TIAToolbox for further analysis due to its open-source nature.

Parameters such as grid spacing and sampling percentages were evaluated for non-rigid registration using TIAToolbox for alignment quality and computational efficiency. Grid spacing 200 and sampling percentage 1.0 show promising results and were used for further investigation into diverse cases which showed successful registration. The thesis also addresses specific challenges encountered in three difficult cases, highlighting the need for continued refinement of the pre-processing pipeline to accommodate complex or damaged tissue sections.

Areas for improvement include automating the pre-processing pipeline, evaluating additional registration tools, and exploring methods beyond pixel-based metrics like IOU and DSC.

Følsomhet Intern (gul)

Further testing on a broader range of WSIs is necessary to comprehensively assess the pipeline's registration success. Future research should address these limitations and integrate the pipeline into a larger framework for the automatic alignment and ordering of biopsy sections, enhancing efficiency for nephropathologists. Overall, this study provides valuable insights into image registration for non-neoplastic kidney biopsy analysis.

1 Introduction

The kidney is a highly intricate organ with vital functions, such as waste excretion, water and salt regulation, acid balance maintenance, and hormone secretion[1]. Non-neoplastic kidney diseases can be classified based on their impact on different kidney components, consisting of glomeruli, tubules, interstitium, and blood vessels[1]. Renal diseases, with their increasing prevalence and significant impact on global health, necessitate efficient and accurate diagnostic methods. Chronic kidney disease (CKD) and its progression to end-stage kidney disease (ESKD) affect millions of people worldwide, often going undetected, due to the kidney's substantial functional reserve, until severe damage has occurred[1-3]. Within European context, CKD affects nearly 100 million Europeans, with 300 million being at risk[4], and is set to become the fifth- leading global cause of death by 2040 and the second leading cause of death before the end of the century in some countries with long life expectancy [5]. This reality underscores the need for advanced diagnostic approaches, particularly in the realm of non-neoplastic kidney disease, a relatively under-researched area.

The integration of digital pathology (DP) represents a transformative advancement in biomedical research and pathology diagnostics because of the possibility to implement AI tools. Utilizing Whole Slide Images (WSI), DP allows for the precise and flexible analysis of tissue samples, transforming traditional microscopy[6, 7]. A key application within this domain is image registration, which involves aligning histology sections using different staining or preparation methods[7]. This technique enables pathologists to overlay or match images from various depths of specimen, ensuring accurate comparisons and comprehensive analysis of tissue structures and cellular features[7]. Consequently, pathologists gain integrated insights into patient pathology, improving the understanding of normal structures and pathological lesions.

Building on recent advancements, this project aims to integrate both commercial and open-source image registration tools into a future pipeline for automating the alignment and ordering of kidney biopsy sections. By leveraging AI techniques such as image registration, this computational image analysis and preprocessing tool seeks to enhance the speed and accuracy of diagnostics in nephropathology, addressing a critical gap in current methodologies. The thesis focuses primarily on image registration in the context of non-neoplastic kidney biopsy sections. The central scientific inquiry revolves around evaluating the performance of these tools in this specific domain. Image registration using non-neoplastic kidney biopsy sections is

currently under-researched, highlighting the need for further investigation. The key question driving this research is: How effectively do image registration tools operate when applied to non-neoplastic kidney biopsy WSIs, and what insights can their evaluation provide for enhancing the quality of image registration for integration into a future larger pipeline?

1.1 Background

1.1.1 Kidney Structures and Diseases

Renal histology focuses on the microscopic anatomy of the kidney, essential for diagnosing kidney diseases [1]. Each human kidney contains about 1.2 million nephrons [8], which are the functional units of the kidney that perform crucial functions in maintaining the body's internal environment [1]. This specific functional element is encompassed in a kidney biopsy[1]. A nephron consists of the glomerulus, which consists of the glomerular tuft and Bowmans's capsule, the renal tubule, which consists of proximal convoluted tubule, the loop of Henle, the distal convoluted tubule, and afferent and efferent arteriole[9]. CKD is a long-term condition characterized by a gradual loss of nephrons and kidney function over time [9]. It can occur due to changes or damage in various kidney structures, including glomeruli, tubules, or blood vessels.

1.1.1.1 Glomerulus

The renal corpuscle (Figure 1) is a crucial component of the nephron responsible for the initial filtration of blood to form urine[10]. It consists of two main structures, the glomerular tuft and the Bowman's capsule[10]. The glomerulus is the site of blood filtration, where waste products and excess substances are removed from the blood to form the initial filtrate[10]. The Bowman's capsule surrounds the glomerular tuft, and it collects the filtrate from the glomerulus and begins the process of urine formation[10].
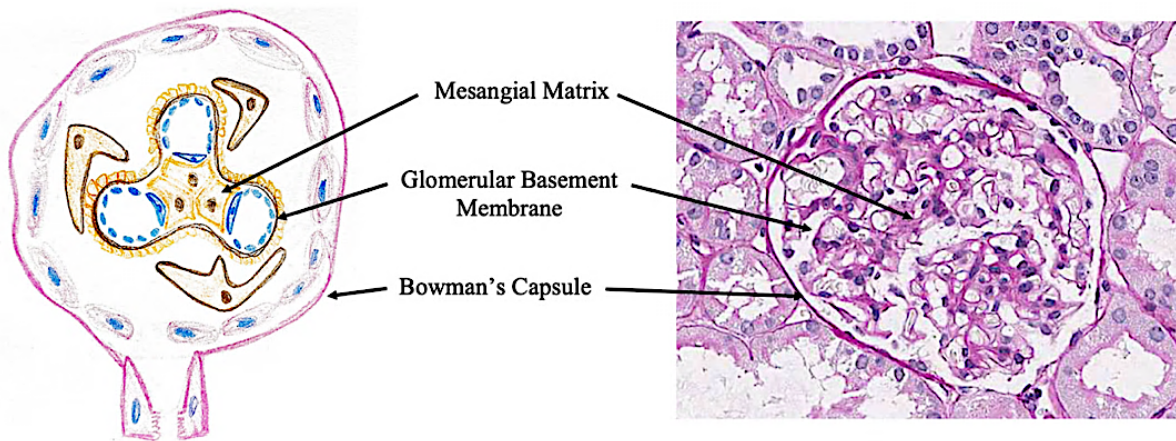
Figure 1 Glomerulus. A sketched and a scanned histology slide representing the glomerular tuft and Bowman's Capsule. The figure shows the Mesangial matrix, Glomerular Basement Membrane, and the Bowman's Capsule. Histology image from: Renal biopsy laboratorium, Department of Pathology, Haukeland University Hospital, Bergen. This graphic was adapted with permission from: Bülow, R. D, et al. (2019)[11]

1.1.1.2 Renal Tubule

The renal tubules (Figure 2) are long, slender tubes that are originated from Bowmans's capsule and are involved in the reabsorption and secretion of substances to fine-tune the composition of urine[12]. It consists of three main structures, the proximal convoluted tubule (PCT), the Loop of Henle, and the distal convoluted tubule (DCT)[12]. The PCT is the first segment of renal tubule, where most of the reabsorption of water, glucose, amino acids, and other essential substances occurs[12]. The Loop of Henle is a U-shaped segment of the renal tubule that plays a crucial role in concentrating urine and maintaining water and electrolyte balance[12]. The DCT follows the loop of Henle and is involved in the further fine-tuning of urine composition through absorption and secretion processes[12]. In addition, the interstitium is the supportive tissue between the glomeruli, tubules, and blood vessels, providing structural support to the kidney[12].
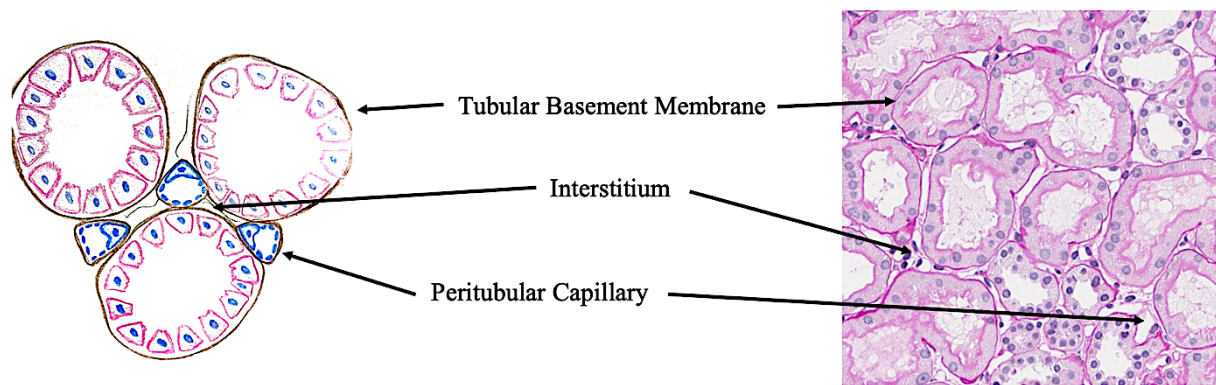
Figure 2 Renal tubules. A sketched and a scanned histology image representing the Renal tubules. Figure shows the Tubular Basement Membrane, Interstitium, and the Peritubular Capillary. Histology slide from: Renal biopsy laboratorium, Department of Pathology, Haukeland University Hospital, Bergen. This graphic was adapted with permission from: Bülow, R. D, et al. (2019)[11]

1.1.1.3   Vasculature

The kidney benefits from a rich blood supply to sustain its essential functions [13]. The renal artery (Figure 3) delivers oxygenated blood to the kidney, where it undergoes filtration within the glomeruli [13]. Subsequently, the filtered blood returns to circulation via the renal vein [13]. Moreover, arterioles play a crucial role in regulating glomerular pressure, thereby contributing significantly to renal function [14]. Arterioles are small blood vessels branching out form arteries and extending into the capillary beds of the kidneys[15]. Within the kidney, arterioles are classified into two primary types: afferent arterioles, supplying blood to the glomeruli, and efferent arterioles, responsible for carrying blood away from the glomeruli[15].
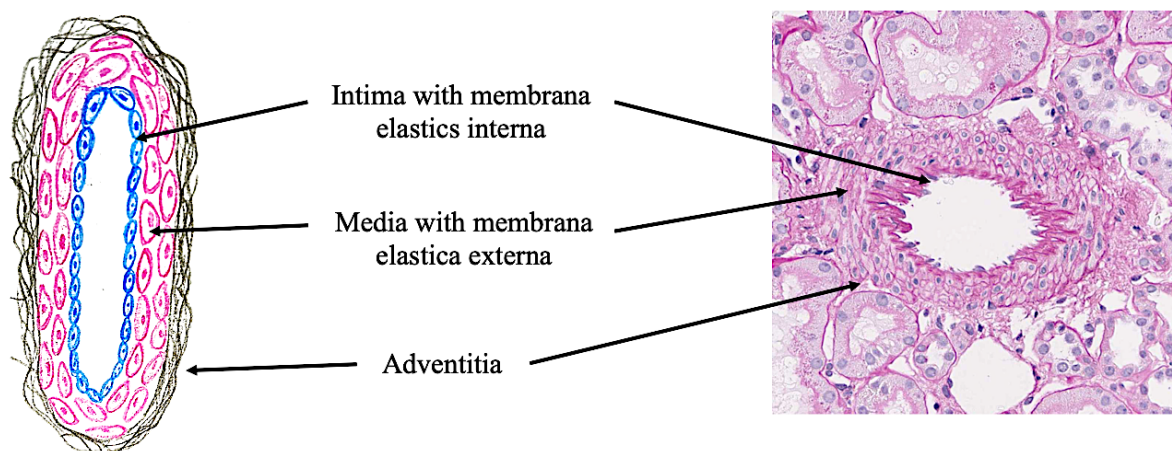
Figure 3 Arterial Vessels. A sketched and a scanned histology image representing the Arterial Vessels. Figure shows the Intima with membrana elastics interna, media with membrane elastics externa, and adventia. Histology image from: Renal biopsy laboratorium, Department of Pathology, Haukeland University Hospital, Bergen. This graphic was adapted with permission from: Bülow, R. D, et al. (2019)[11]

1.1.1.4 Kidney Diseases

Kidney diseases encompass three primary categories: neoplastic (including cancers), non-neoplastic, and transplant pathology. This project focuses on utilizing WSI from non-neoplastic kidney diseases. Non-neoplastic kidney diseases are grouped based on compartments of origin: glomerular diseases, tubulointerstitial diseases, and diseases affecting kidney blood vessels. Understanding the interconnectedness between compartments is important. Issues in one compartment can impact others, underscoring the importance of accurate diagnosis to prevent complications and ensure effective treatment. Kidney diseases can in addition be categorized as primary or secondary diseases with primary diseases originating within the kidney and secondary forms arising from systemic conditions. The distinction between primary and secondary forms of kidney disease is important to the clinician as it has implications for prognosis and treatment.

1.1.2 Nephropathology

1.1.2.1 Diagnosing

Diagnosing kidney disease involves a combination of clinical evaluation, blood, and urine tests, and sometimes imaging or biopsy.[9] Blood tests assess the levels of creatinine and urea to estimate the glomerular filtration rate (GFR), which indicates how well the kidneys are filtering waste.[9] Urine tests can detect albumin, signalling possible damage of filtration units. Imaging like ultrasounds can reveal the size and structure of the kidneys, while a biopsy provides a direct look at kidney tissue health.[9] These methods together allow clinicians to diagnose the presence, type and stage of kidney disease, as well as to guide treatment decisions.[9]

1.1.2.2 Biopsies and Biopsy Evaluation

Kidney biopsies stand as an important diagnostic procedure, offering insights at microscopic level of kidney tissues. This process involves the retrieval of a minute tissue specimen from the kidney, which is then examined under a microscope. Histopathological evaluation of the biopsy can reveal distinct abnormalities, such as scarring, inflammation, or specific deposits, crucial for diagnosing various renal diseases[9]. This detailed tissue analysis not only provides accurate disease identification but also informs prognosis and guides therapeutic strategies, making it an essential component in the management of patients with serious kidney disease.[9]

1.1.2.3 Pathology Workflow

The processing of kidney biopsies for histopathological analysis is a detailed and labour – intensive procedure. An overview of the pathology laboratory workflow producing these sections is presented in figure 4. It begins with a radiologist or nephrologist extracting a small tissue sample using a biopsy needle. This sample is immediately preserved in fixatives such as formalin to maintain structural integrity. The tissue is then dehydrated, cleared, and embedded in paraffin wax for thin sectioning. Thin sections of 3μM are cut using a microtome and placed onto glass slides with adhesive. These sections undergo staining, such as Haematoxylin and Eosin (H&E), Periodic acid-Schiff (PAS), Masson's Trichrome, immunohistochemistry, among others. The final step involves securing the stained tissue with a coverslip for microscopic examination. Subsequently, the glass slides are scanned and converted to WSIs. Each step is crucial for rendering a correct diagnosis, highlighting the importance of maintaining high quality throughout the entire process. When the kidney biopsy is received by the biomedical laboratory scientists, it is divided into two parts. The larger portion undergoes paraffin embedding, sectioning, and staining to visualize tissue structures and cellular morphology, or immunohistochemistry to detect specific proteins or antigens within the kidney tissue sections, such as immune complexes in glomeruli. The smaller portion is processed for electron microscopy. The tissue is embedded in EPON which allows for cutting very thin sections for electron microscopic investigation providing high-resolution imaging of cellular structures and detailed information about kidney cell morphology (Figure 5). The data used for this project are from paraffin-embedded slides.
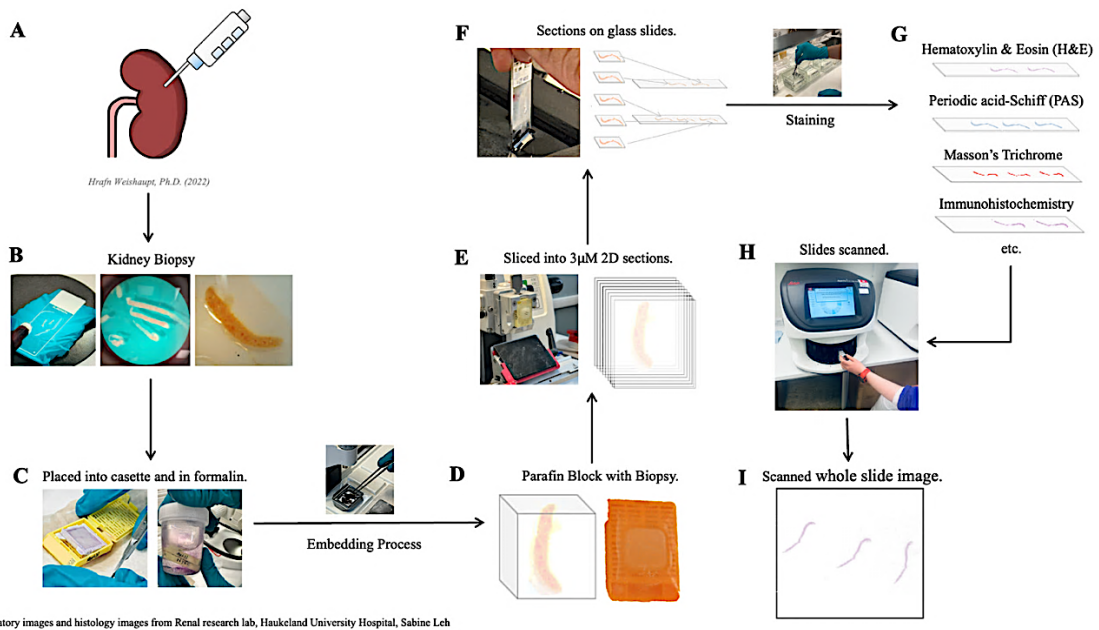
Figure 4 Pathology workflow for kidney biopsy analysis by light microscopy. A) Nephrologist or radiologist takes kidney biopsy. B) Biopsy needle cores received by nephropathology lab. C) Tissue placed in cassettes, immersed in formalin. D) Biopsy undergoes embedding, forming paraffin block. E) Thin 3 µM sections cut using microtome. F) Sections stretched and attached to glass slides using hot water bath. G) Glass slides stained using various techniques. H) Stained slides scanned. I) WSI generated. Image source: Renal biopsy laboratory, Dept. of Pathology, Haukeland Univ. Hospital, Bergen.
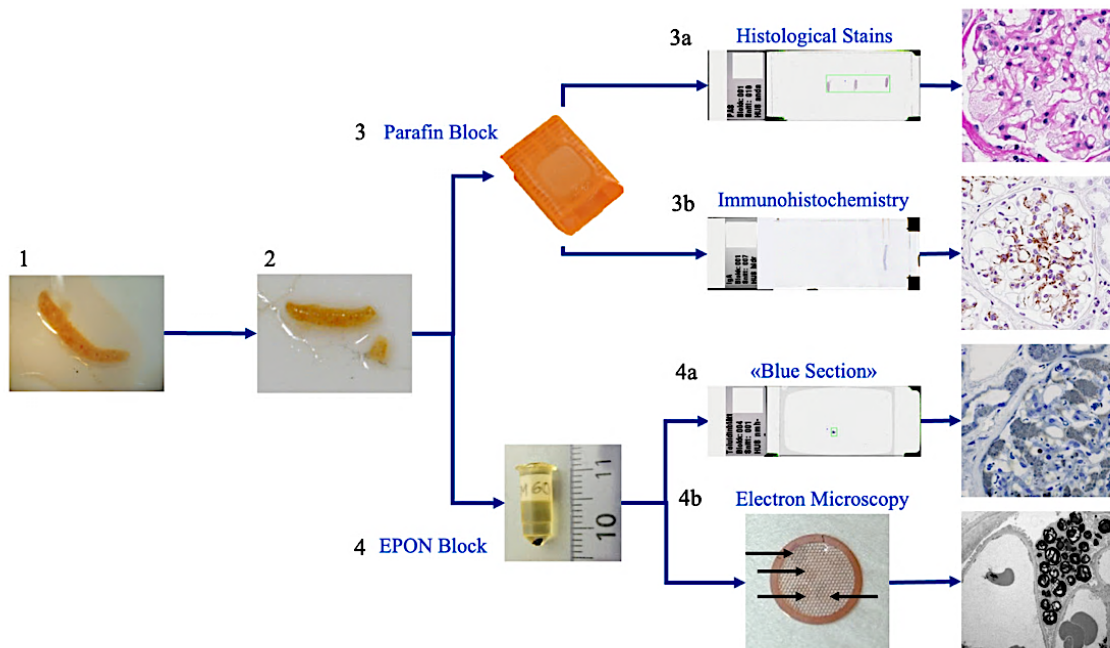
Figure 5 Kidney Biopsy work-up including electron microscopy. The kidney biopsy process involves several key steps: 1) Initial biopsy acquisition: A nephrologist retrieves the kidney biopsy specimen, which is then delivered to the nephropathology laboratory. 2) Biopsy division: The specimen is divided into two parts. 3) The larger portion undergoes paraffin embedding and sectioning, which includes: 3a) Histological stains to visualize tissue structures and cellular morphology, and 3b) Immunohistochemistry, enabling the detection of specific proteins or antigens within the kidney tissue sections, such as immune complexes in glomeruli. 4) The smaller biopsy part is embedded into EPON: 4a) First the EPON block is utilized for semithin sectioning, highlighting tissue structures, and aiding in identifying areas of renal abnormalities suitable for electron microscopic investigation. 4b) Second, the EPON block is trimmed, and ultrathin sections are cut for electron microscopy, providing high-resolution imaging of kidney structures and detailed information about kidney cell morphology. These processes are essential for accurate diagnosis and are conducted at the Renal biopsy laboratory, Dept. of Pathology, Haukeland University Hospital, Bergen. (Sabine Leh, MD, PhD.)

1.1.3 Nephropathology in the Digital Era

Over the past decade, the perception and application of virtual microscopy have undergone significant changes. Initially considered an emerging technology with limited applications in primary diagnostics, its use was mainly confined to educational settings, largely due to traditional pathologists' preference for conventional light microscopy[16]. However, with the advent of scanned WSIs (seen Figure 4 H-I), the field of pathology has experienced a remarkable transformation with the emergence of digital pathology. This innovation enables the effective utilization of slide and image archives that were previously underexploited, presenting opportunities for research and diagnostic precision.

Digital pathology offers several advantages. Firstly, it enhances workflows by eliminating bottlenecks, such as dispatching cases to pathologists or archiving slides, allowing labs to handle larger caseloads efficiently while reducing turnaround times[17]. Secondly, it standardizes staff training through digital resources, ensuring consistent, high-quality education for pathologists[17]. Collaboration is greatly facilitated through telepathology, as digitized samples eliminate the need for physical slides, allowing for seamless remote consultation and education[17]. The digital format also enables deeper insights through high-quality viewing and AI-assisted analysis using computational image analysis and software, revealing patterns and markers that might be missed with traditional methods[17]. Overall, the digitization of pathology not only streamlines existing processes but also paves the way for innovative technologies like AI to further enhance patient care and research[17]. This also applies for nephropathology, as kidney structures are considered complex. The use of digital pathology, along with AI-assisted analysis, will save time and make diagnoses for nephropathologists more efficient.

1.1.3.1 Digital Pathology

DP is rapidly transforming clinical pathology practice and laboratory settings, serving as a cornerstone for modernized medical workflows[16, 18-20]. The utilization of scanned histological slides integrates digital workflow and imaging solutions, facilitating the acquisition, management, interpretation, and scrutiny of digital formats for specific content[16]. The availability of digital slides enables a range of functions including remote primary diagnostics, teleconsultation, workload management, collaborative efforts, centralized clinical trial assessments, image analysis, virtual education, and pioneering research endeavors[19]. Through

the utilization of WSI technology, computer vision and artificial intelligence (AI) communities have expanded computational pathology capabilities[19].

Europe was at the forefront of developing digital pathology (DP), with several institutions pioneering its adoption. Kalmar County Hospital in Sweden was the first in Europe to adopt digital pathology, starting in 2006 to improve ergonomics by reducing microscope usage[21]. Since 2008, Kalmar and Linköping University Hospital have scanned over 500,000 glass slides for routine operations[21]. In 2014, the pathology department in Førde, Norway, demonstrated that digital pathology could address increased workload, case complexity, financial constraints, and staffing shortages efficiently and reliably[22]. Bergen, also in Norway, began using digital pathology for nephropathology in 2012 (Sabine Leh, MD, PhD). In 2015, the University Medical Centre in Utrecht, The Netherlands, implemented a fully digital workflow for primary diagnostics within six months, creating a complete digital archive[23]. That same year, Cannizzaro Hospital in Catania, Italy, transitioned to a fully digital pathology workflow using WSI[24]. In 2016, Granada University Hospitals in Spain adopted full digital pathology for primary diagnosis, digitizing all histopathology slides at ×40 magnification using the Philips IntelliSite Pathology Solution[25].

In the USA and Canada, digital pathology research predates widespread implementation, which awaited FDA approval of commercial WSI platforms[16, 26]. Nonetheless, the adoption of digital pathology has been substantial, with practices transitioning beyond traditional image archiving to comprehensive digital solutions[16].

Advances in computing power, network speeds, and storage affordability have further propelled the efficiency and flexibility of managing digital slide images, promoting digital pathology applications in telepathology, clinical trials, education, and research[18]. The benefits of digital pathology, including time-efficient review processes and advanced image analysis tools, promise a more objective and consistent diagnostic framework, reshaping the future of pathology[16, 18].

1.1.3.2 Digital Nephropathology

Digital pathology has emerged as a transformative tool in nephropathology, leveraging advancements in technology to enhance diagnostic processes and improve patient care. The widespread adoption of scanners and the integration of WSIs alongside traditional glass slides have made nephropathological diagnostics more efficient[27]. With the digitization of renal biopsy slides, pathologists and nephropathologists can remotely access and analyze images, facilitating real-time consultations and expediting diagnostic decision-making[28]. Moreover, digital pathology platforms enable standardized acquisition and storage of WSIs, creating a valuable resource for educational purposes[28]. Trainees and practicing pathologists benefit from access to a comprehensive digital archive of annotated cases, facilitating learning and proficiency assessment. Additionally, digital nephropathology enable advanced image analysis and quantitative assessment of renal biopsy specimens[28]. Machine learning algorithms can be trained to recognize histological patterns and quantify various renal pathologies, including glomerular lesions, tubulointerstitial fibrosis, and vascular changes[18, 29]. By automating these tasks, digital pathology reduces the burden of manual image interpretation and enhances the reproducibility of diagnostic assessments. Furthermore, the integration of AI into digital pathology workflows holds promise for improving prognostic stratification and treatment decision-making in nephropathology[28].

1.1.3.3 Challenges in Digital Pathology

The transition to digital pathology presents multifaceted challenges for healthcare institutions, both technically and organizationally[30]. This transition, while, promising, requires a bespoke approach as the digital infrastructure and strategy that may suit one institution could be inadequate for another [30]. Critical decisions regarding the extent of digitization, such as whether to adopt a fully digital framework or to convert only specific segments of slide collections is important. These decisions not only dictate the technological needs, including the type and volume of scanners required based on expected slide throughput and desired processing speeds, but also define the overarching digital workflow[30]. In addition to hardware considerations, the shift towards digital pathology extends into significant IT resource requirements, particularly in terms of data storage and computational power. An institution generating 1,600 biopsy slides daily, with each slide approximately 2 GB in size, must anticipate the need for more than 1 petabyte of storage capacity each year to manage this data effectively[30]. The need for high storage systems and expertise represents a significant financial investment[31].

1.1.4 Image Analysis

1.1.4.1 Computational Image Analysis

The fusion of advanced scanning technology and the growing availability of extensive digital image datasets has created collaboration between pathologists and technology specialists such as data scientists, computational engineers, and imaging physicists[16]. The aim here is the extraction and quantification of data from digital images, either standalone or combined with other biological or omics data, to unveil insights not accessible through traditional methods. AI and Machine Learning (ML) excel in dissecting complex datasets to identify underlying patterns and features within histopathological images that are beyond the scope of traditional visual inspection (eyeballing)[16]. Deep learning (DL), a subset of ML characterized by multi-layered neural networks, further enhances this capability, enabling in-depth examination of WSIs for tasks such as detection, segmentation, and classification with great precision[16]. In nephrology and nephropathology, AI -powered tools promise to enhance the understanding of kidney disease heterogeneity and outcomes, offering significant enhancements over existing classification systems[16].

1.1.4.2 Image Recognition in Digital Pathology

Image recognition in digital pathology is the process of automatically identifying and classifying features in digital images. In digital nephropathology, this technique is applied in various scenarios, illustrated by examples in the following section. To classify glomerular lesions a three-step workflow might be used (Figure 6A)[32]. Firstly, glomeruli are detected in biopsy images using a trained HALO AI (Indica Labs) classifier model[32]. Secondly, the detected glomeruli images are centred within a 1024 x 1024 pixel-sized patch, a non-glomerulus background pixels are discarded[32]. Thirdly, pre-processed glomeruli are classified using three approaches: multiple binary classifiers in a one-vs-rest setting, a single multiclass classifier, and a spatially guided multiclass classifier[32]. These classifiers are trained using a five-fold cross-validation setting[32]. The output is a set of classified glomeruli instances and corresponding attention heatmaps[32]. The study compares the three classification approaches using classification accuracy and area under the curve (AUC) metrics, and evaluates neural attention visualizations (heatmaps) against nephropathologists' annotations using intersection over union (IOU) metrics[32]. Another application involves training a deep learning model to

quantify fibrosis in non-neoplastic kidney biopsies (Figure 6B)[33]. This process begins with tissue sections stained with Haematoxylin and Eosin (H&E). After destaining, these sections are stained with Sirius Red[33]. Conventional image analysis is then used to create masks of the Sirius Red-stained fibrosis areas[33]. These masks train a deep learing algorithm to measure fibrosis in the corresponding H&E-stained sldies[33]. The model's performance is validated using F-statistics[33]. A further application is the automatic detection of glomeruli with subsequent automatic measurement of glomerular size described in a study in male obese BTBR *ob/ob* mice[34]. Glomeruli were automatically detected and segmented from WSIs using the HistoCloud tool[35].
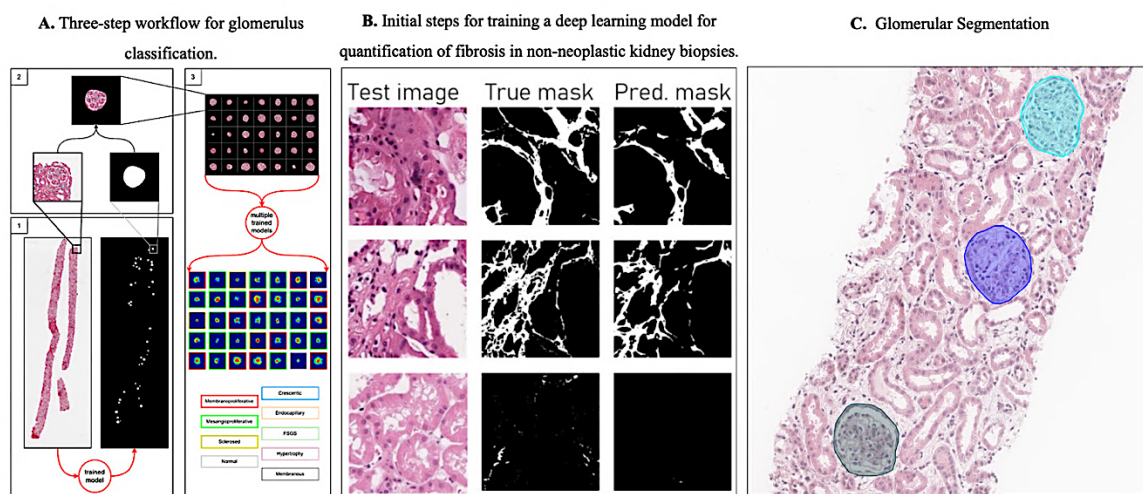
Figure 6 Image Recognition in Digital Nephropathology. This figure demonstrates applications of image recognition with examples. (A) The three-step workflow for glomerulus classification involves: (1) detecting glomeruli in biopsy images using a trained HALO AI (Indica Labs) classifier model; (2) centering detected glomeruli images within a 1024 x 1024 pixel-sized patch and discarding non-glomerulus background pixels; (3) classifying pre-processed glomeruli using three different approaches: multiple binary classifiers in a one-vs-rest setting, a single multiclass classifier, and a spatially guided multiclass classifier, all trained using a five-fold cross-validation setting[32]. This figure is with permission from: Besusparis, J., Morkunas, M., & Laurinavicius, A. (2023). A Spatially Guided Machine-Learning Method to Classify and Quantify Glomerular Patterns of Injury in Histology Images. J Imaging, 9(10). doi:10.3390/jimaging9100220 (B) Fibrosis segmentation was performed as a proof of concept to detect fibrosis in H&E stains (predicted mask). For comparison, the true mask generated on Sirius red stains is also shown[33]. This graphic is with permission from: Mola N, Hodneland E, Weishaupt H, Leh S, editors. Training a deep learning model for quantification of fibrosis in non-neoplastic kidney biopsies - a feasibility study. 34th European Congress of Pathology; 2022; Switzerland, Congress Center Basel. (C) The figure depicts glomerular segmentation using image recognition techniques. (Weishaupt H, (2024). Glomerular Segmentation.)

1.1.4.3   Image Registration in Digital Pathology

There are many situations in the evaluation of WSIs in which the individual sections need to be aligned with each other to enable the pathologist to view multiple WSIs simultaneously. The term for image alignment is image registration. Image registration involves aligning two

or more images, which can be from the same or different sources: one designated as the fixed or reference image and the other as the moving image[36]. The moving image undergoes spatial transformation to align it with the fixed image. This process is frequently a preliminary step in various medical image analysis procedures. Image registration in digital pathology serves three functions: enabling cross-slide image analysis, facilitating multimodal image fusion, and supporting the three-dimensional reconstruction of tissues from serial histological sections[36]. These functionalities collectively enhance the integration and interpretation of histological information, offering a more holistic understanding of tissue architecture and pathology, thus significantly contributing to advancements in medical diagnostics and research methodologies[36].

There are two main methods for automatic image registration: intensity -based registration and feature-based registration[36]. In intensity-based registration, the method focuses on the brightness or colour of the pixels in the images[36]. It tries to adjust the moving image so that its pixels match up as closely as possible with the fixed image by measuring how similar the two images are and adjusting until they align well. On the other hand, feature-based registration looks for specific parts of the images, like edges or corners, and uses these as landmarks[36]. The process finds these landmarks in both images and then lines them up by figuring out the best way to fit them together. The choice between the two methods depends on the nature of the images[36]. The registration techniques discussed above primarily involve linear methods, where the moving image is moved through basic transformations like flipping, rotating, or shifting to align with the fixed image. However, due to deformation occurring during histological processing, non-linear registration methods are also necessary for alignment. Currently, non-linear methods for histology images are under research. One proposed non-linear registration method is by TIAToolbox, which utilizes a B-spline transform. This deformable registration method employs B-spline curves to define a continuous deformation field. Enabling precise mapping of each pixel in the moving image to its corresponding pixel in the fixed image[37].

1.2 Problem

Conducting image registration in histology images presents two primary challenges. Firstly, WSI are vast, often exceeding 10 gigabytes of uncompressed storage size per image. Some images even surpass 80 gigabytes in memory size. Addressing the challenge of processing such large-scale data and complex computations requires the utilization of high-performance

computing systems. Alternatively, a pre-processing step involving downscaling and reducing the number of pixels can be employed. However, this approach risks altering the original data obtained in the laboratory. To prevent alteration of the original laboratory data, one can develop a pipeline and test it using downscaled images before applying it to full-scale images with the aid of high-performance computing systems. Secondly, challenges arise from the susceptibility of kidney tissue to deformation throughout histological processing, leading to changes in tissue dimensions. These alterations can introduce inaccuracies when aligning images from different sections. To address this issue, non-linear compensation methods are employed to resolve the registration problem.

Moreover, direct registration of kidney biopsy sections using raw data from is not feasible with existing image registration tools. Prior to registration, raw images typically have to undergo a series of pre-processing steps, which deal e.g. with the segmentation of tissue, the selection of reference and target sections for alignment, dealing with stain variation, etc. These include managing variations in the number of sections in histology images (Figure 7), accounting for the presence of control tissue, and accommodating differences in tissue staining and thickness. These steps are essential to ensure accurate and reliable image registration. Therefore, achieving accurate image registration in kidney histopathology requires consideration of tissue characteristics, staining methods, and computational resources. By addressing these challenges, we can ensure the precision and utility of registered images for diagnostic and research purposes.
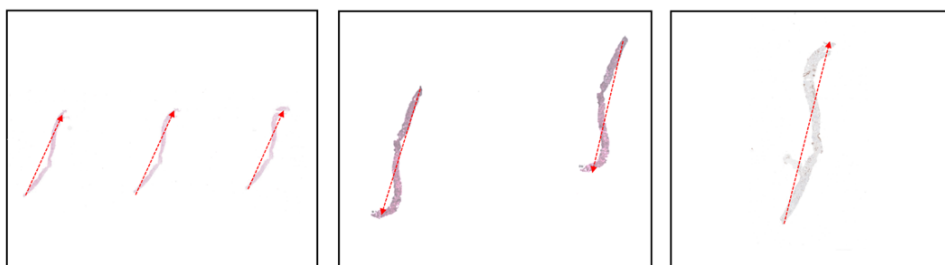

Figure 7 Scanned Whole Slide Images. The whole slide images depict biopsy sections that are not perfectly ordered or oriented. Red arrows indicate the direction in which the sections are pointing. Histology images from Renal research lab, Haukeland University Hospital, Sabine Leh.

1.3 Related Works

Lotz et al.'s study compares consecutive and restained sections, highlighting the importance of deformable registration methods in histopathology[38]. While consecutive sections allow cost-effective region-level annotations, restained sections offer superior nucleus-level alignment for biomarker analysis[38]. This research, closely aligned with commercial HistokatFusion tool, provides valuable insights for optimizing image registration in diagnostic and research contexts[38]. Additionally, limitations are discussed, including the reliance on landmarks as the measure of accuracy and the need for comprehensive evaluation metrics[38]. The study acknowledges challenges in assessing smoothness of deformation and discrepancies between datasets due to various factors[38].

Awan et al., in collaboration with Lotz, investigate registering multiple sections within a tissue block, crucial for cross-slide image analysis[36]. Their focus on non-rigid registration methods, particularly using Deep Feature Based Registration a rigid registration method as a primary approach, achieves precise alignment with minimal errors[38]. The development of a visualization tool enhances workflow efficiency[38]. This research, associated with the open-source tool TIAToolbox, offers valuable insights into optimizing registration processes for histopathological analysis[38].

1.4 Open Questions?

Despite considerable advances in histopathological image registration, there is still a substantial lack of research regarding the use of such technology in the field of nephropathology. Firstly, can these tools be directly applied to raw data obtained from histology laboratories? Secondly, how well do current non-rigid methods work, and how do they impact tissue interpretability after registration? Additionally, how do the resolution and quality of histology images impact the accuracy of image registration? Moreover, what role do variations in staining techniques play in influencing the performance of image registration algorithms? Lastly, what is the performance of already available open-source and commercial image registration tools when applied to kidney images, and how easily can they be adopted for such an application?

2 Aim and Objectives

The current project is part of an endeavour to develop a future pipeline to automatically align randomly positioned biopsy sections into an ordered sequence (Figure 8). The pipeline will consist of two main components: 1) image registration and 2) consecutive section ordering based on when the section was cut using microtome. This thesis will primarily focus on the first component, namely the image registration phase. The project will unfold in two distinct stages, each corresponding to a specific objective. The first objective will involve identifying suitable image registration tools, whether commercial or open source through literature review. The second objective involves implementing and evaluating these tools, which will lay the foundation for future efforts to integrate them into a fully functional pipeline, facilitating the larger organizational process.
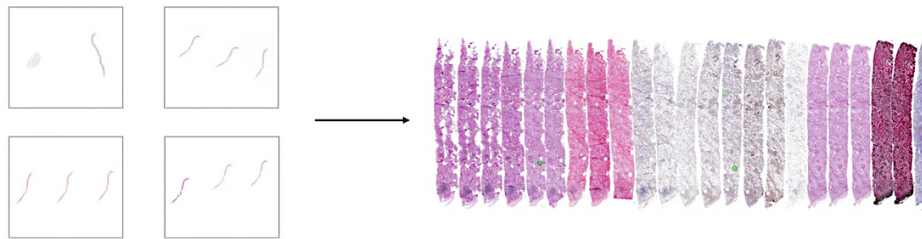
Figure 8 Software tool designed to align and order kidney biopsy sections. This figure depicts the objective of the extended pipeline. It involves extracting sections from kidney biopsy whole slide images and arranging them in a coherent sequence.

Creating a tool capable of automatically arrange randomly positioned biopsy sections into an ordered sequence offers several advantages. Firstly, it enables nephropathologists to gain a better understanding of pathological lesions based on kidney structures, such as glomeruli (Figure 9). Additionally, this approach streamlines the diagnostic process, as pathologists can efficiently review all sections aligned side by side in the correct order, eliminating the need to open new slides for each section.
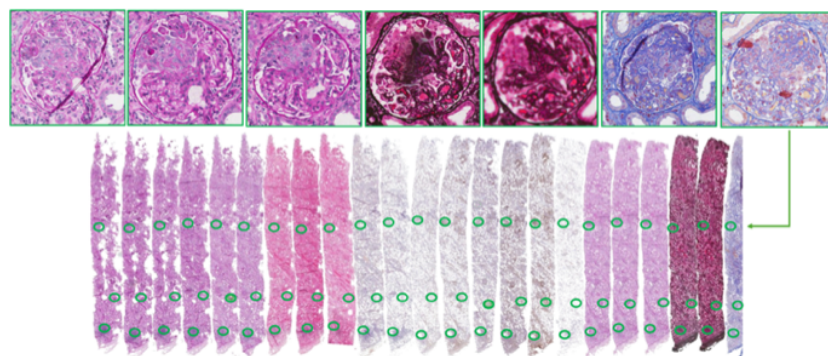
Figure 9 Comprehensive visualization of kidney structures. The figure illustrates how the result produced by the software tool might look like. The image showcases how easily one specific glomerulus can be tracked through all sections. In addition, serial images (or views) of the glomerulus can be depicted side by side, allowing for in-depth analysis and examination of renal morphology.

3 Part I - Literature Review

3.1 Materials and Methods

In this literature review, a search strategy was implemented to identify relevant image registration tools that can be integrated into the pipeline. Electronic databases, PubMed and IEEE Xplore, were systematically searched using predetermined keywords and search filters. For PubMed, the search phrase was: "(image registration) AND (digital pathology) AND (Whole Slide Images)" (Table 1). Studies were included based on predefined criteria, including publication in academic conferences, relevance to the research topic, availability in the English language, and publication within the past 5 years, and included articles from 2019 to 2024. Exclusion criteria encompassed non-peer-reviewed sources, lack of direct relevance to the research topic, and non-English language publications.

Table 1 Summary of PubMed Search Criteria and Results.

Criteria	Details
Search Database	PubMed
Search Terms	(image registration) AND (digital pathology) AND (Whole Slide Images)
Filters Applied	Publication Date: Last 5 years
Date of Search	11.09.2023
Number of Results	26
Selection Criteria	English Language
Total Articles Selected for Review	10
Selected For Detailed Review	2

For IEEE Xplore, the search phrase was: ("All Metadata": image registration) AND ("All Metadata": digital pathology) (Table 2). Studies were included based on predefined criteria, including publication in academic conferences, relevance to the research topic, availability in the English language, and included period from 2015 - 2024. Exclusion criteria encompassed non-peer-reviewed sources, lack of direct relevance to the research topic, and non-English language publications. Strengths of the review methodology included the comprehensive search strategy and rigorous selection criteria, while limitations encompassed potential publication bias and language restrictions.

Table 2 Summary of IEEE Xplore Search Criteria and Results.

Criteria	Details
Search Database	IEEE Xplore
Search Terms	("All Metadata": image registration) AND ("All Metadata": digital pathology)
Filters Applied	2015- 2024
Date of Search	11.20.2023
Number of Results	57
Selection Criteria	English Language
Total Articles Selected for Review	4
Selected For Detailed Review	3

Following a literature review, five articles were chosen for further analysis, identifying six image registration tools (Table 3). A Google search was conducted to assess the user-friendliness, past successful utilization, and predominant dataset usage (e.g., radiology data or histology images) for each tool.

3.2 Results

After conducting a thorough review of relevant literature and considering various factors, including user-friendliness, past successful applications, and predominant dataset (e.g., radiology data or histological images), it was decided to utilize two tools: HistokatFusion and TIAToolBox. HistokatFusion, being a commercial tool, was noted for its intuitive interface and widespread adoption among researchers, thereby facilitating user- friendliness and successful utilization in previous studies. On the other hand, TIAToolBox, as an open-source tool, was found to have a user-friendly manual. Additionally, its code was accessible and easily adaptable. Both tools were employed for the analysis of histological images, aligning well with the requirements of the study.

Table 3 Selected Literature for Detailed Review from Literature Review.

Article Title	Authors/Year	Findings	Commercial/Open-Source
'Comparison of consecutive and restained sections for image registration in histopathology'[38]	Lotz, J., et al. (2023)	HistokatFusion	Commercial
'SimpleElastix: A User-Friendly, Multi-lingual Library for Medical Image Registration'[39]	Marstal, K., et al. (2016)	SimpleElastix	Open-Source
'elastix: a toolbox for intensity-based medical image registration'[40]	Klein, S., et al. (2010)	Elastix	Open-Source
'ANHIR: Automatic Non-rigid Histological Image Registration Challenge'[41]	Borovec, J., et al. (2020)	ANTs (Advanced Normalization Tools)	Open-Source
'ANHIR: Automatic Non-rigid Histological Image Registration Challenge'[41]	Borovec, J., et al. (2020)	NiftyReg	Open-Source
'Deep feature based cross-slide registration'[36]	Awan, R., et al. (2023)	TIAToolBox	Open-Source

4 Part II

This section outlines the practical application of the commercial and open-source image registration tools HistokatFusion and TIAToolbox.

4.1 Materials and Methods

The system configuration utilized for this study consisted of a 14-inch MacBook Pro (2023) powered by an Apple M2 Pro chip, equipped with 16GB of RAM, and running macOS Sonoma 14.0.

A summary overview of the workflow is depicted in figure 10. The pre-processing phase involved down-sampling and segmentation of the raw images into individual sections. Registration was conducted using both the commercial tool HistokatFusion and the open-source tool TIAToolBox. With HistokatFusion, the fixed and moving images were uploaded to the server and registered. In contrast, TIAToolBox[36] employed a structured framework designed to enhance registration accuracy. This framework encompasses three primary stages: initial pre-processing, establishing rigid alignment via the Direct Feature-Based Registration (DFBR) approach, and subsequent nonlinear registration using B-Spline transform, all facilitated by TIAToolBox.

The registration success and comparison will be assessed using the intersection over union and dice score metrices.

The code for accomplishing the tasks described in this section was developed partially with the help of ChatGPT[42].

PRE - PROCESSING

Downscaled Raw Image   **Tissue Segmentation**   **Section Extraction**

REGISTRATION

Fixed Image

Moving Image

Commercial

HistokatFusion
Correlating Histopathology

Open-Source

TIA Centre
TISSUE IMAGE ANALYTICS

TIA Toolbox 1.4.1

Upload in Server.   Registered Image

Rigid Transformation   Non – Rigid Transformation

Deep feature based cross-slide
Registration (DFBR)

B-Spline Transform

EVALUATION

Registered Image

Intersection Over Union (IOU) $= \dfrac{Area\ of\ overlap}{Area\ of\ union} = \dfrac{|A \cap B|}{|A \cup B|} =$

$|A \cap B|$

$|A \cup B|$

Dice Score (DSC) $= \dfrac{2 \times Overlap}{Total\ Area} = \dfrac{2|A \cap B|}{|A| + |B|} =$

$|A \cap B|$

Figure 10 Workflow Summary. This figure presents an overview of the thesis's whole workflow, encompassing the preprocessing of Whole Slide Images (WSIs), image registration, and evaluation methods. Initially, WSIs undergo down sampling before tissue segmentation and division into individual sections for subsequent processing. These downscaled images are then uploaded to the HistokatFusion server for registration. For the open-source tool, TIAToolbox, the images undergo rigid registration utilizing deep feature-based registration (DFBR), followed by non-rigid registration using B-spline transform. The resultant registration outcomes are then compared and evaluated using Intersection over Union (IOU) and Dice Score (DSC) metrics.

4.1.1 Image Pre- Processing

All WSIs used in this project were obtained from the Renal Biopsy Laboratory, Department of Pathology, Haukeland University Hospital, Bergen. The image pre-processing procedure is divided into three main phases: pre-processing of raw images, extraction of tissue section images, and pre-processing of tissue section images.

4.1.1.1   Pre-processing of Raw Images

In the initial phase, the raw data underwent a down-sampling process, reducing its size by a factor of 16 - 18 for all except WSI_6 (Table 4 and Figure 12A). Figure 11 shows an example of the downscaling process for WSI_6. The image was downscaled by 40% and then by an additional 10x. The 40% downscaling was chosen because the system configuration could only process a 40% downscaled image for WSI1_6. WSI1_6 images are used to compare the two image registration tools.
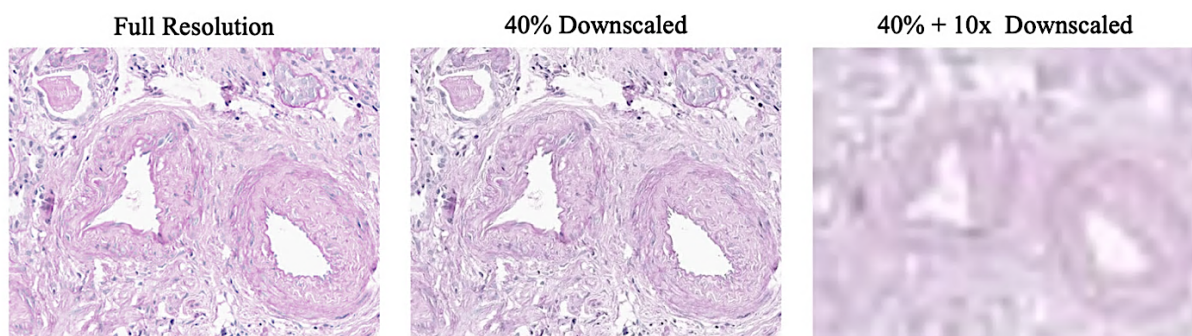
Figure 11 Visualization of images at different resolutions. Full resolution, 40% downscaled, and 40% downscaled with an additional 10x downscaling. The WSIs depict vasculature structure at three different resolutions.

4.1.1.2   Extraction of Tissue Section Images

Subsequently, segmentation was performed using code sourced from TIAToolbox (Figure 12B). However, modifications were made to this code to accommodate certain sections requiring an additional connected component for segmentation. Consequently, the sections were separated into individual connected components or segments (Figure 12C). The number and selection of connected components required for detection were manually determined for each WSI. Subsequently, bounding boxes were computed for each segment (Figure 12D) and the respective coordinates were then applied in the original image (Figure 12E) to extract individual segments as separate images in TIFF format (Figure 12F).

Følsomhet Intern (gul)

Figure 12 Pre-Processing of Raw Data. All raw data were downscaled by a factor of 16 except WSI_6 from case no.1 presented in illustration above, which was downscaled by 40% (A). This downscaled image was tissue segmented. (B). The s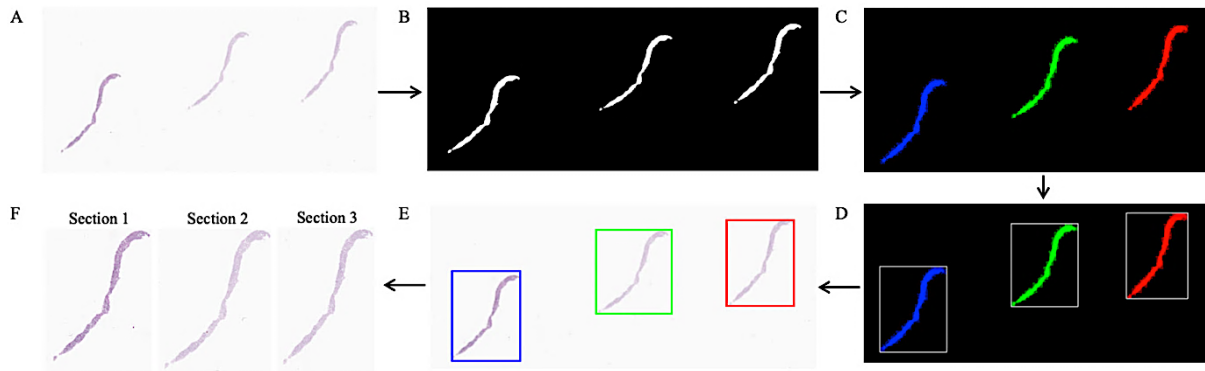egmented white pixel sections were all divided into separate connected components indicated as blue, green, and red (C). Bounding boxes were placed around the connected components (D). The bounding boxes were then applied to the original downscaled image (E) to crop out the sections into individual TIFF images (F).

4.1.1.3   Pre-processing of Tissue Section Images

In the second phase of the process, the selection of the fixed image was conducted based on various criteria, including structural integrity, image quality, and suitability for all sections within the WSI (Figure 12A). Structural integrity implies that images were chosen to display similar anatomical structure across all sections of the WSI, as shown in figure 13. Image quality of each section was also assessed, considering potential contaminations such as dust and debris, staining artifacts, tissue folding or wrinkling, air bubbles, glass imperfections, and other factors.
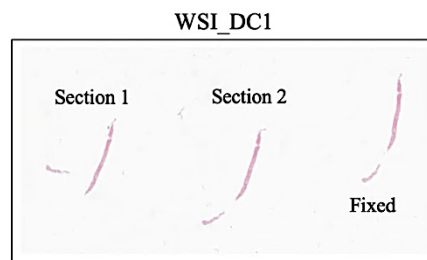
Figure 13 Example of Structural Integrity. Fixed images in WSI_DC1 chosen to be the section with the most structural integrity, as the section appears like section 2. In section 1, the smaller broken part is shifted.

Prior to registration with TIAToolbox, images underwent preprocessing, during which some images were downscaled by a factor of 2 to 3, depending on their size. The selection of the moving image was randomized among the sections not chosen as the fixed image (Figure 14A). Segmentation of both the fixed and moving images was performed using code modified from TIAToolbox (Figure 14B). To ensure uniform dimensions and facilitate accurate alignment image padding was conducted to the fixed and moving images as well as their corresponding

masks (Figure 14C-D). Furthermore, the masks underwent thorough validation to ensure complete binary representation (Figure 14D).
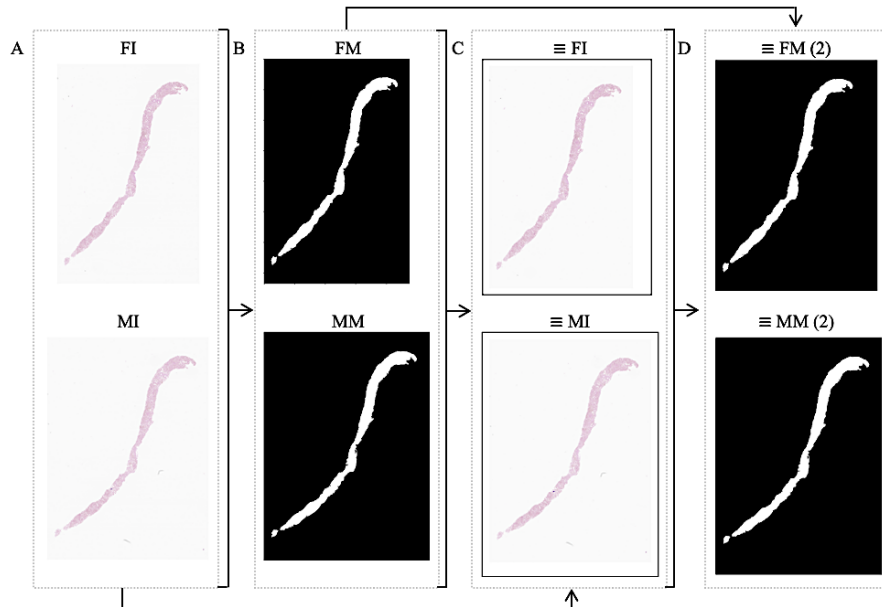
Figure 14 Pre-Processing for Registration. Moving and fixed images were again downscaled by a factor of 3 (A). Segmentation of both the fixed and moving images was conducted using code modified from TIAToolbox (B). Added image padding to the fixed and moving images, as well as their corresponding binary masks (C-D).

Table 4 Downscaling factor for each registered WSIs.

Case no.	WSI	Downscaling Factor
Case 1	WSI1_6	40%
	WSI1_11	18x
	WSI1_12	18x
Case 2	WSI2_1	16x
Case 3	WSI3_1	18x
Case 4	WSI4_1	16x
Case 5	WSI5_1	18x
Case 6	WSI6_1	17x
Case 7	WSI7_1	17x
Case 8	WSI8_1	17x
Case 9	WSI9_1	17x
Case 10	WSI10_1	17x
Case 11	WSI11_1	17x

4.1.2 Rigid and Non-Rigid Registration

The TIAToolbox image registration algorithm comprises a two-step registration process involving rigid and non-rigid registration. Initially, the fixed and moving images undergo a pre-alignment process known as rigid or linear registration. Rigid registration primarily entails rotating, flipping, or shifting the moving image to align with the fixed image (Figure 15A). However, since histological sections may undergo deformations during processing, rigid registration alone is insufficient. Hence, a non-rigid or non-linear alternative become necessary. This non-rigid approach allows the moving image to deform itself to better match the fixed image, accommodating the deformations encountered during histological processing (Figure 15B).
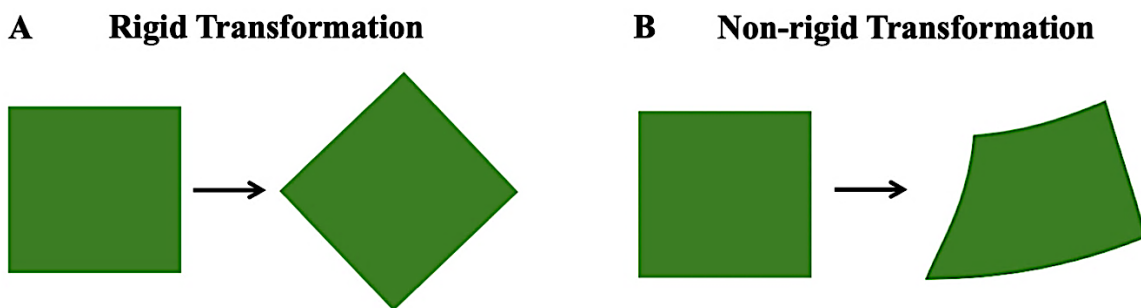
Figure 15 Rigid and Non-Rigid Transformation. (A) Rigid Registration enables images to rotate, flip, or shift the moving image to align with the fixed image. (B) Non-rigid registration allows the moving image to deform itself to better match the fixed image.

4.1.2.1   Rigid Registration (Deep Feature Based Registration)

The pre-processing stage lays the groundwork for image registration results by initially generating a tissue mask for each image pair and standardizing the image dimensions of fixed and moving images. Following this, the Deep Feature Based Registration (DFBR) method was utilized to achieve an initial alignment. DFBR employs data-driven descriptors to estimate the global transformation [36], enabling linear alignment through flipping and rotating the sections. This process utilizes both the fixed and moving images, along with their respective masks, to obtain a rigid transformation result (Figure 16).
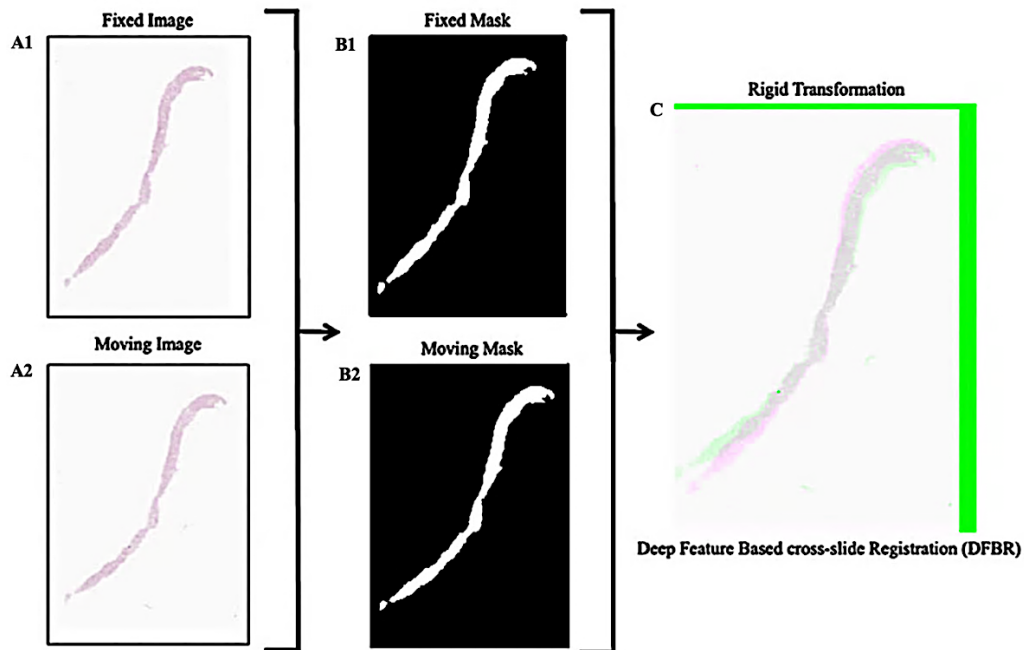
Figure 16 Rigid-Transformation using DFBR. For rigid transformation, both fixed and moving images were segmented to obtain binary masks. Fixed image is indicated in pink and registered image is indicated in green. The grey area is the overlap between fixed and registered images. The green borders indicate additional padding added to the moving image after registration to make the dimensions the same.

4.1.2.2 Non – Rigid Registration using B- Spline Transform

After rigid transformation, the fixed and rigid-registered images, along with their corresponding masks, are utilized as input for obtaining a non-rigid transformation result (Figure 17). Non-rigid registration is achieved using B-Spline Transform, which is one of the default algorithms for non-rigid registration available in TIAToolbox and is a deformable registration method employing B-spline curves[37]. To ensure precise alignment, two parameters, the grid spacing and the sampling percentage, were carefully adjusted. The default settings typically include a grid spacing of 50 and a sampling percentage of 0.2.

33
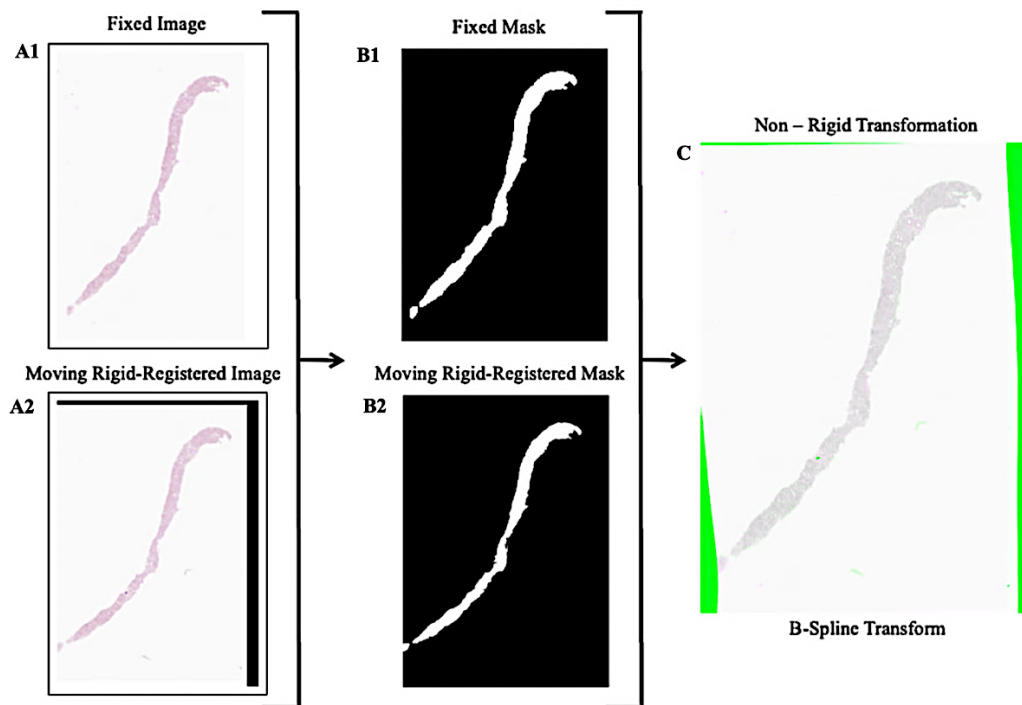
Figure 17 Non-Rigid Transformation using B-Spline Transform. For non- rigid transformation, fixed and the moving rigid-registered images are segmented into binary masks and registered. The grey area represents the overlap between the fixed and registered images. In the non-rigid transformation results, the green borders indicate additional padding added to the moving image after registration to ensure the dimensions match. For the moving rigid-registered image, this padding is black.

The grid spacing is defined as the distance between gridlines. Coordinates of crossing gridlines hitting the tissue section are control points (Figure 18). These control points serve as references for aligning two images. The sampling percentage value denotes the proportion of the detected section utilized for image registration. To determine the optimal grid spacing and sampling percentage values for non-neoplastic kidney biopsy WSI, various parameter values were tested on WSI_12 from case no-1 to evaluate their effects on alignment results.

Figure 18 Grid- Space with control points. This image illustrates grid overlaid on a section, where the spacing between each gridline represents the grid spacing. Each intersection between grid lines acts as a control point.

4.1.2.3 Visualization of Registration Results

The registration output was visualized consistently across all registered sections. For HistokatFusion (Figure 19A), an overlay of the fixed image in green and the moving image in purple was presented, allowing the transformation to be observ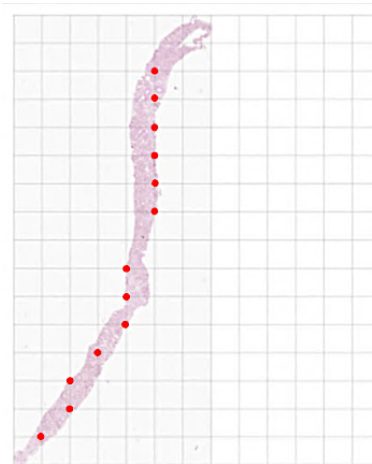ed through the shapes of the resultant image. For TIAToolbox (Figure 19B), the visualization included the fixed image in pink and the registered image in green. The grey area indicates the overlap between the fixed and registered images. The green borders highlight the extra padding added to the moving image post-registration to ensure dimension matching.
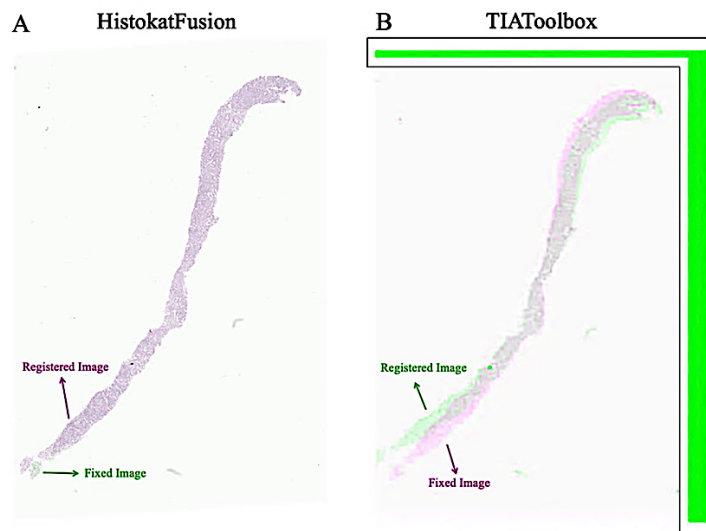
Figure 19. Visualization of Registration Output. (A) The registration output for HistokatFusion shows an overlay of the fixed image (green) and the moving image (purple), allowing the transformation to be observed through the shapes of the resultant image.[43] (B) The registration output for TIAToolbox displays the fixed image (pink) and the registered image (green). The grey area indicates the overlap between the fixed and registered images. Additionally, green borders denote the extra padding added to the moving image after registration to ensure the dimensions matched.[44]

4.1.3 Intersection Over Union (IOU) and Dice Score (DSC)

To compare the open-source tool TIAToolbox and the commercial tool HistokatFusion, a statistical analysis is conducted using Intersection over Union (IOU) (Equation 4.2.4.1) and Dice Score (DSC) (Equation 4.2.4.2) to obtain objective metrics. The statistical analysis involves utilizing fixed and registered binary masks. Subsequently, the coordinates of white pixels in the masks are determined. From these pixel coordinates, the intersection and union are computed, enabling the computation of IOU and DSC values (Figure 20).

4.2.4.1. $\quad Intersection\ Over\ Union\ (IOU) = \dfrac{Area\ of\ overlap}{Area\ of\ union} = \dfrac{|A \cap B|}{|A \cup B|} = \dfrac{Counted\ white\ pixels\ (overlap)}{Counted\ white\ pixels\ (union)}$

4.2.4.2 $\quad Dice\ Score\ (DSC) = \dfrac{2 \times Overlap}{Total\ Area} = \dfrac{2|A \cap B|}{|A|+|B|} = \dfrac{2 \times Counted\ white\ pixels\ (overlap)}{Counted\ white\ pixels\ (Fixed) + Counted\ white\ pixels\ (overlap)}$
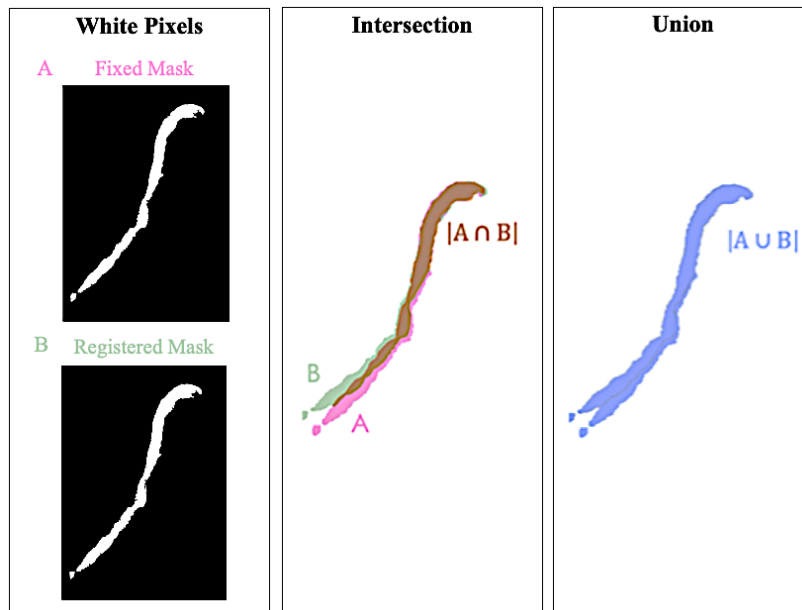
Figure 20 Intersection Over Union (IOU) and Dice Score (DSC). The method used to calculate IOU and DSC involves using binary fixed and registered masks to determine the coordinates of the white pixels. These coordinates are then used to compute the IOU and DSC metrics based on the displayed equations for IOU and DSC formulas. (Refer in figure text.)

4.1.4 Image Pre- Processing for Broken Sections

The pipeline was also tested on challenging cases. When dealing with a challenging WSI, it might exhibit issues such as a broken section, as illustrated in figure 21. To address issues such as broken sections, during pre-processing, individual components are again automatically identified as part of the tissue segmentation procedure. Subsequently, where applicable, if a single section consisted of multiple components (either due to broken tissue or multiple tissue cylinders), these were manually combined by labelling them as belonging to the same section. Following this, a bounding box is then computed for each set of merged components and the coordinates are utilized to crop the respective regions from the raw image. The individual images that have been separated are subsequently employed for additional image registration utilizing TIAToolbox.
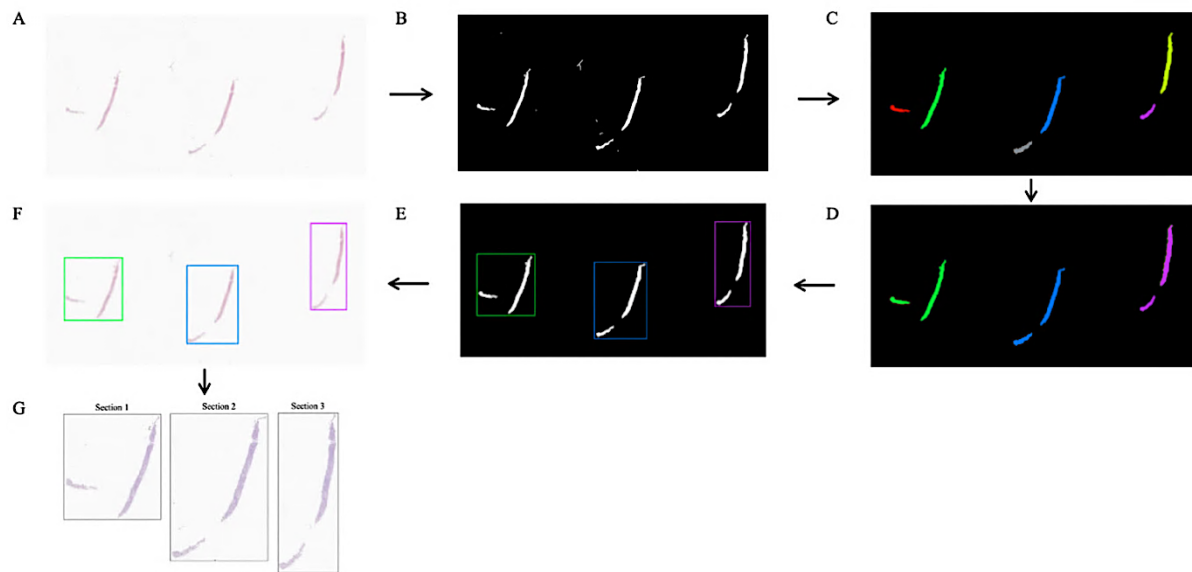
Figure 21. Pre-Processing of raw data for difficult cases. A) The raw data undergoes down-sampling by a factor of 16. B) Subsequently, the downscaled image undergoes tissue segmentation. C) The segmented sections are then separated into distinct connected components. D) Certain components are then merged to form new combined components. E) Bounding box coordinates are applied to surround the combined connected components. F) The bounding boxes computed for these merged components are then utilized to crop the respective regions from the raw image. G) Individual TIFF files for each section are extracted from the original image.

4.2 Results

4.2.1 Comparison Between HistokatFusion and TIAToolBox

Given the limited memory resources available in the utilized computing environment/setting, to be able to utilize TIAToolbox, both the fixed and moving images underwent downscaling from 40% to an additional down-sampling by a factor of 10 to facilitate the registration process. HistokatFusion was capable of registering images at a higher resolution; however, to enable a comparison with TIAToolbox, images with the same resolution were used.

Based on visual examination, the image registration outcomes achieved with HistokatFusion appears promising (Figure 22). However, upon closer inspection at the microscopic level, imperfections are evident in the lower parts of the sections, indicating incomplete alignment. This discrepancy is illustrated in figure 22, where arrow demonstrate the imperfect alignment in zoomed-in view.
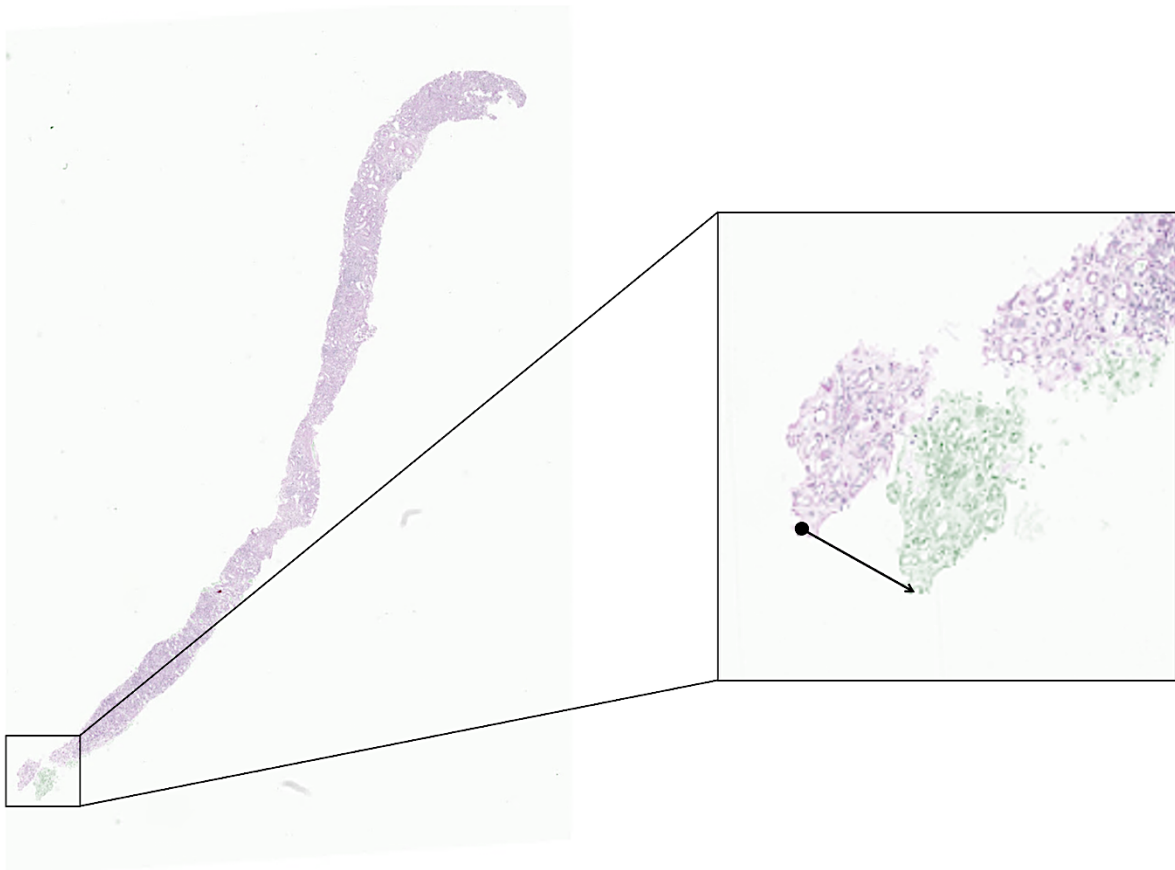
Figure 22 Registration results obtained with HistokatFusion. The registration appears successful across most areas, except for a specific region highlighted in the zoomed-in view, where discrepancies between the fixed and registered images are visible. In the illustration, green represents the fixed image, while purple indicates the registered image.[43]

Registration using TIAToolbox was also conducted, starting with a rigid transformation followed by a non-rigid transformation. The registration appeared successful based on visual inspection; however, achieving precise registration at a microscopic level was hindered due to the downscaling of images. Nonetheless, at a less magnified scale, the results were satisfactory (Figure 23).

Rigid Transformation   Non – Rigid Transformation

Deep feature based cross-slide Registration (DFBR)   B-Spline Transform
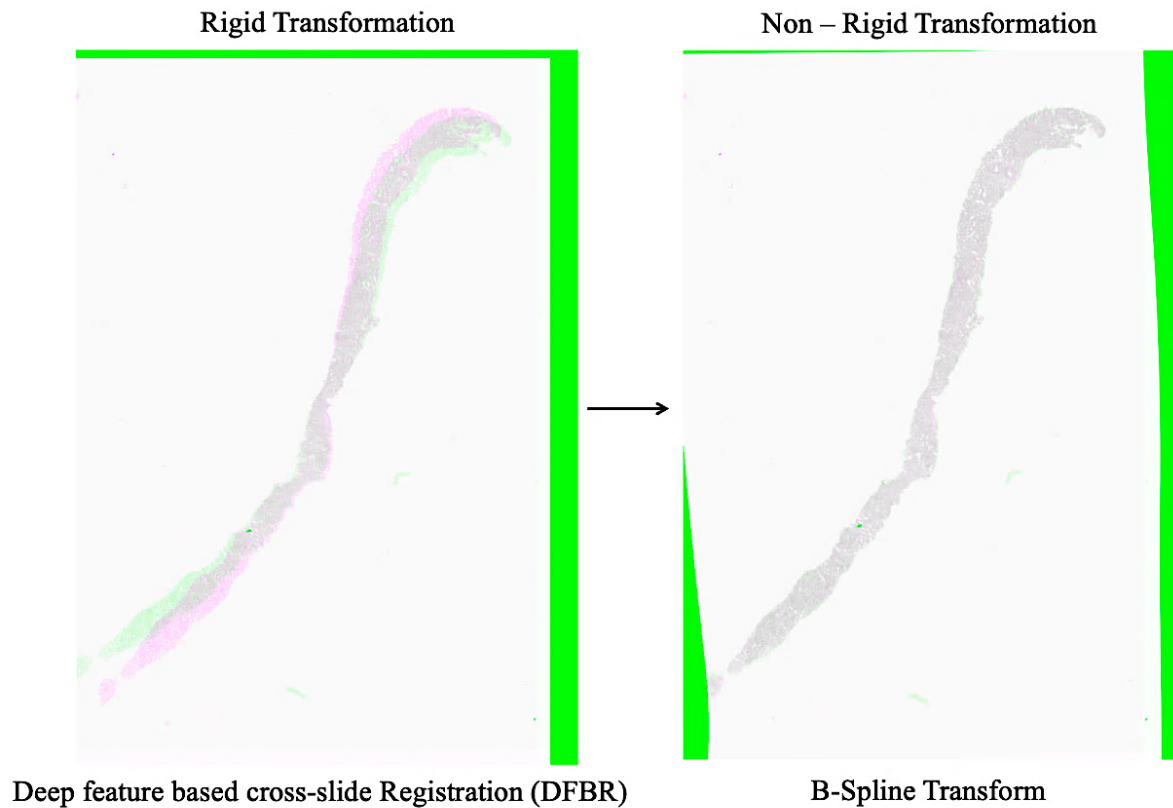
Figure 23 Registration using TIAToolbox. The fixed and moving images undergo segmentation and registration using both rigid and non-rigid transformations. Fixed image is indicated in pink and registered image is indicated in green. The grey area is the overlap between fixed and registered images. Additionally, green borders denote the extra padding added to the moving image after registration to ensure the dimensions matched.[44]

Intersection over Union (IOU) and Dice Score (DSC) metrics were employed to evaluate the registration results of a single WSI (WSI1_6), which underwent a 40% down sampling and an additional 10x scaling (Table 5). HistokatFusion (Figure 22) achieved an IOU of 0.94 and a DSC of 0.97, while TIAToolbox (Figure 23) showed an IOU of 0.88 and a DSC of 0.93. Although HistokatFusion, a commercial tool, demonstrated higher IOU and DSC metrics, TIAToolbox, being an open-source tool, was selected for further testing. This decision was influenced by its potential for (1) further refinement through parameter optimization to enhance performance and (2) easier integration into larger pipelines due to its open-source nature. Consequently, TIAToolbox was employed for registration testing across diverse and challenging cases.

Table 5 Intersection Over Union (IOU), Dice Score (DSC), and downscaling factor.

Tool/Software	WSI	Downscaling Factor	Intersection over Union (IOU)	Dice Score (DSC)
HistokatFusion	WSI_6	40%	≈ 0.96	≈ 0.98
HistokatFusion		40%, additional 10x	≈ 0.94	≈ 0.97
TIAToolBox		40%, additional 10x	≈ 0.88	≈ 0.93

4.2.2 Testing of Various Grid Space and Sampling Percent Values

Based on the high IOU and DSC values observed in the initial testing on a single image (WSI1_6) integrating TIAToolbox into a broader pipeline for automated alignment and ordering appears feasible. However, further testing on a variety of sections is needed, as the pipeline might not yield the same level of registration on other WSIs beyond the one used for initial testing. For instance, discrepancies in registration may arise due to inherent differences among WSIs, which stem from variations introduced during histological processing, such as differing amounts of cylinders per section, broken sections, stain variations, etc. Consequently, the pipeline was applied to different whole slide images to ascertain if any modifications to the code are necessary.

Towards this end, the project started with an evaluation of the parameter values used during registration. Specifically, for the grid spacing and sampling percentage parameters, TIAToolbox utilizes default values of 50 mm and 0.2, but it is unclear whether these values would provide the best results for the kidney biopsy sections presented here. Accordingly, to evaluate the impact of these parameters, an experiment was conducted on WSI1_12, repeating the registration multiple times systematically testing different combinations of grid spacing and sampling percentage values. Factors considered when evaluating the choice of these parameter values included achieving the best alignment based on the IOU and DSC, as well as computational time (Table 6).

Table 6 Test of Grid Space and Sampling percent values for best alignment results.

Case no.	WSI	Grid Space	Sampling Percent	IOU	DSC	Computational Time
Case 1	WSI1_12	200	0.1	≈ 0.93	≈ 0.97	≈ 4.23s
			0.2	≈ 0.94	≈ 0.97	≈ 6.93s
			0.3	≈ 0.95	≈ 0.97	≈ 8.17s
			0.4	≈ 0.95	≈ 0.98	≈ 10.2s
			0.5	≈ 0.95	≈ 0.98	≈ 11.0s
			0.6	≈ 0.96	≈ 0.98	≈ 13.7s
			0.7	≈ 0.95	≈ 0.98	≈ 15.5s
			0.8	≈ 0.95	≈ 0.98	≈ 17.5s
			0.9	≈ 0.96	≈ 0.98	≈ 20.8s
			1.0	≈ 0.96	≈ 0.98	≈ 21.1s
		100	0.1	≈ 0.91	≈ 0.96	≈ 6.36s
			0.2	≈ 0.95	≈ 0.97	≈ 8.90s
			0.3	≈ 0.94	≈ 0.97	≈ 12.9s
			0.4	≈ 0.95	≈ 0.98	≈ 16.4s
			0.5	≈ 0.95	≈ 0.98	≈ 17.3s
			0.6	≈ 0.96	≈ 0.98	≈ 17.6s
			0.7	≈ 0.96	≈ 0.98	≈ 16.6s
			0.8	≈ 0.95	≈ 0.98	≈ 18.8s
			0.9	≈ 0.96	≈ 0.98	≈ 20.1s
			1.0	≈ 0.96	≈ 0.98	≈ 23.2s
		50	0.1	≈ 0.88	≈ 0.94	≈ 11.2s
			0.2	≈ 0.94	≈ 0.97	≈ 17.6s
			0.3	≈ 0.95	≈ 0.97	≈ 18.7s
			0.4	≈ 0.95	≈ 0.97	≈ 20.0s
			0.5	≈ 0.95	≈ 0.98	≈ 22.4s
			0.6	≈ 0.95	≈ 0.98	≈ 23.8s
			0.7	≈ 0.95	≈ 0.98	≈ 27.7s
			0.8	≈ 0.95	≈ 0.98	≈ 24.8s
			0.9	≈ 0.95	≈ 0.98	≈ 37.2s
			1.0	≈ 0.96	≈ 0.98	≈ 39.4s
		20	0.1	≈ 0.93	≈ 0.96	≈ 48.6s
			0.2	≈ 0.92	≈ 0.96	≈ 77.7s
			0.3	≈ 0.93	≈ 0.97	≈ 75.2 s
			0.4	≈ 0.93	≈ 0.96	≈ 89.0s
			0.5	≈ 0.86	≈ 0.93	≈ 92.8s
			0.6	≈ 0.86	≈ 0.93	≈100s
			0.7	≈ 0.86	≈ 0.92	≈ 91.6s
			0.8	≈ 0.79	≈ 0.88	≈128s
			0.9	≈ 0.75	≈ 0.86	≈141s
			1.0	≈ 0.75	≈ 0.86	≈137s

The visual representations in figure 24 depict a comparative analysis of alignment outcomes across various grid spacings, namely 200, 100, 50, and 20, each paired with different sampling percentages. The findings indicate that grid spacings of 200, 100, and 50, when complemented by higher sampling percentages, yield better IOU and DSC results compared to a grid spacing of 20. In figure 25, a graphical depiction of computational time plotted against sampling percentage across various grid space values is presented. Notably, the visualization illustrates that higher grid spacings coupled with lower sampling percentages result in reduced computational time. Specifically, grid space 200 demonstrates the shortest computational time, albeit with marginal differences observed between grid spacings 200, 100, and 50. Conversely, grid spacing 20 exhibits a significantly larger disparity in computational time compared to the other parameters values. After considering computational efficiency and alignment quality, a grid spacing of 200 mm and a sampling percentage of 1.0 appeared to offer the best registration among the tested parameter choices coupled to a reasonable computational time frame. Consequently, these parameters were adopted for any downstream analyses on the remaining sections.

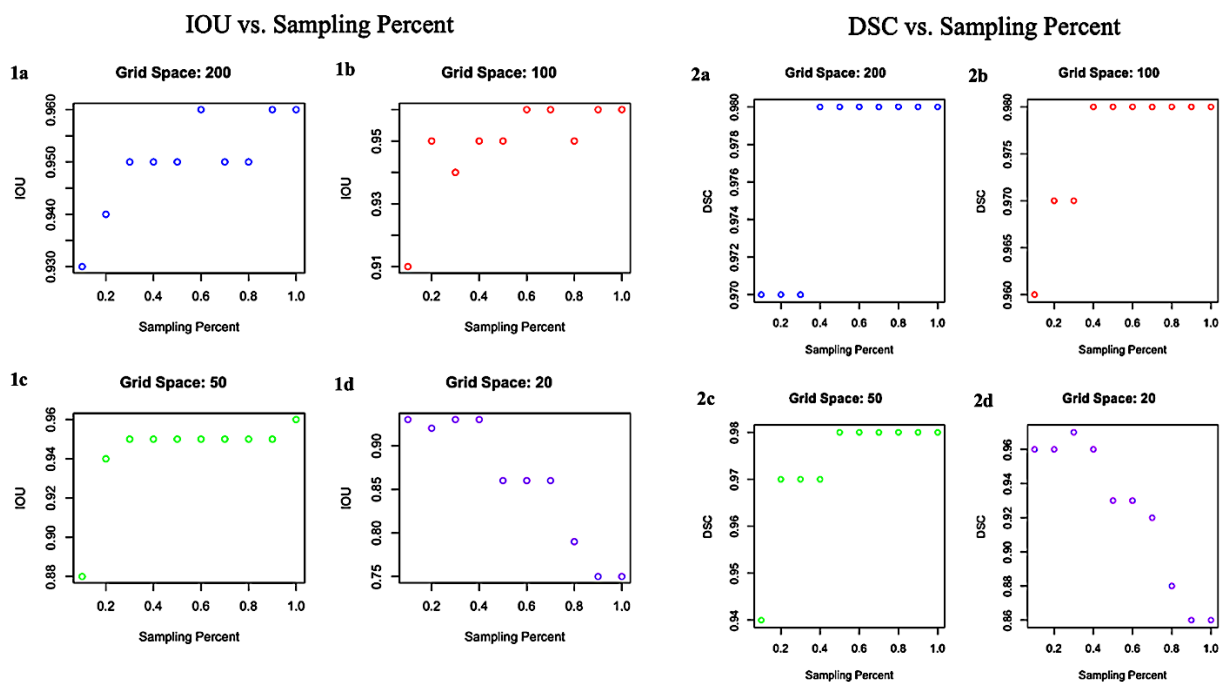**Figure 24 Grid Space and Sampling Percent for IOU and DSC.** 1a-d) Scatterplots illustrating IOU values plotted against sampling percentages for different grid spaces: 200 (a, blue), 100 (b, red), 50 (c, green), 20 (d, purple) on the left side. 2a-d) Scatterplots illustrating DSC values plotted against sampling percentages for different grid spaces: 200 (a, blue), 100 (b, red), 50 (c, green), 20 (d, purple) on the right side.
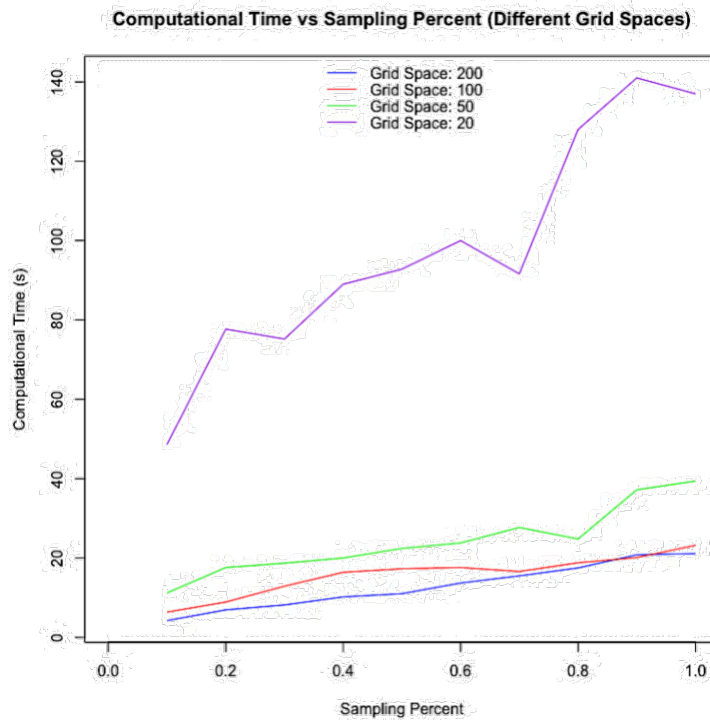
Figure 25 Computational Time vs. Sampling Percent and Grid Space. The line diagram displays the computational time required for each registration run across varying sampling percentages for different grid spaces (200 in blue, 100 in red, 50 in green, and 20 in purple).

The IOU/DSC for grid spacing 200 and sampling percentage 1.0 is approximately 0.93/0.97, while for grid spacing 20 and sampling percentage 1.0, it is approximately 0.75/0.86. Figure 26 visualizes the contrast in registration quality between these scenarios. For grid spacing 20 (Figure 26B), the intersection area tends to get smaller, and noise appears in the white intersection area of the mask, resulting in poorer registration outcomes. One explanation for this outcome may be that the increase in control points as grid spacing decreases poses challenges for the algorithm in accurately detecting relevant points crucial for precise registration. As the number of control points increases, the likelihood of noise, which refers to random fluctuations in the data that may not represent the true underlying patterns[45], also increases.

44

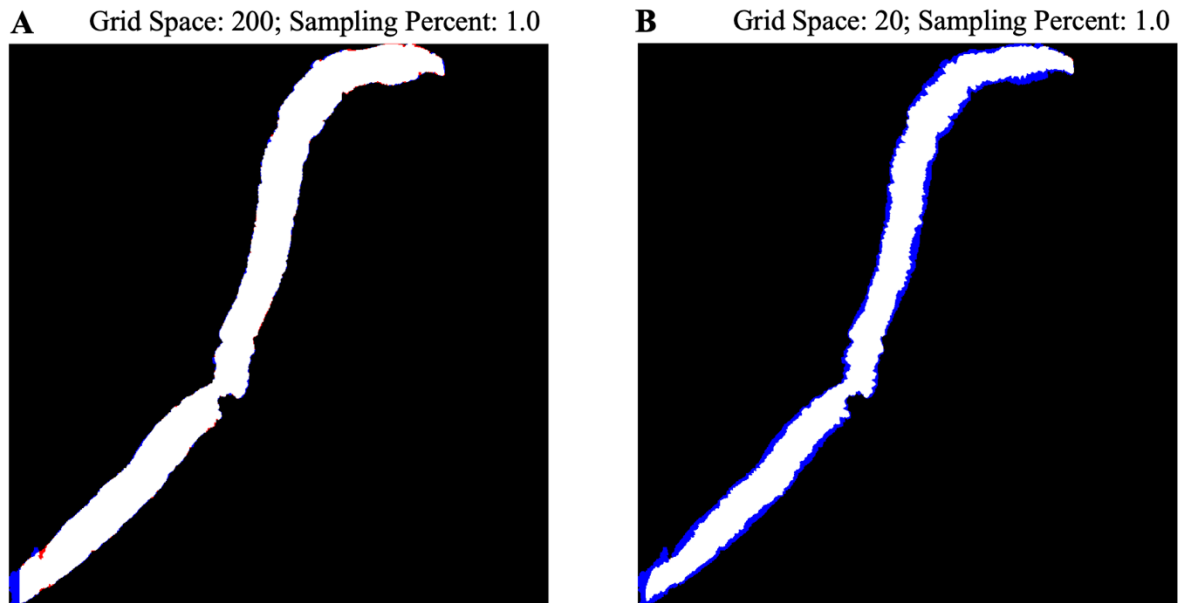**Figure 26 Visualization of the mask registration results for two scenarios.** The figure presents registration results for grid spacings of 200 (A) and 20 (B), respectively, both with a sampling percent of 1.0. The images depict the overlay of the masks of the fixed and registered images, where blue pixels represent the region of the overlay unique to the fixed image, the red pixels represent the region of the overlayed mask unique to the registered image, and the white pixels indicate the intersection of the fixed and registered masks. This color – coding highlights the overlap and discrepancies between the two masks, providing a visual representation of the registration accuracy.

4.2.3 Application of TIAToolbox on Diverse Sections

The pipeline underwent testing using a diverse set of 12 WSIs, each exhibiting unique characteristics. This set was specifically chosen to test the adaptability of the pipeline and to investigate whether and which types of adjustments are necessary to approach general applicability. The adjustments made to the pipeline included employing different pre-processing techniques to handle the specific features and variation present in each WSI. This section details the registration results, categorized by WSIs with individual sections, sections with several cylinders, and sections that exhibit distinct structural differences, highlighting the effectiveness and limitations of the pipeline.

4.2.3.1   WSIs with One Biopsy Cylinder

The registration results for WSIs with individual sections demonstrate that the pipeline can be adapted to work on WSIs with various types of structural appearances and possible challenges. WSI1_11 (Figure 27) underwent successful registration with a satisfactory outcome, achieving

an IOU/DSC of 0.93/0.96. WSI1_12 (Figure 28) exhibited good registration results, with an IOU/DSC of 0.95/0.98. Both WSI8_1 (Figure 29) and WSI4_1 (Figure 30) showed successful registration, with IOU/DSC results of 0.91/0.95 and 0.69/0.82, respectively. Adjustments to the pipeline were made to accommodate variations in structural characteristics, such as gaps within sections, which may have influenced the registration outcome. Nevertheless, visual inspection suggests that the registration is satisfactory.

Figure 27 Image registration results for WSI1_11. On the left-hand side, the WSI includes selected fixed and moving images. Images are registered through both rigid transformations using DFBR (middle) and non-rigid transformations using B-spline transform (right side). The green section indicates the fixed image, and the pink section shows the registered image. Additionally, green borders denote the extra padding added to the moving image after registration to ensure the dimensions matched.[44]
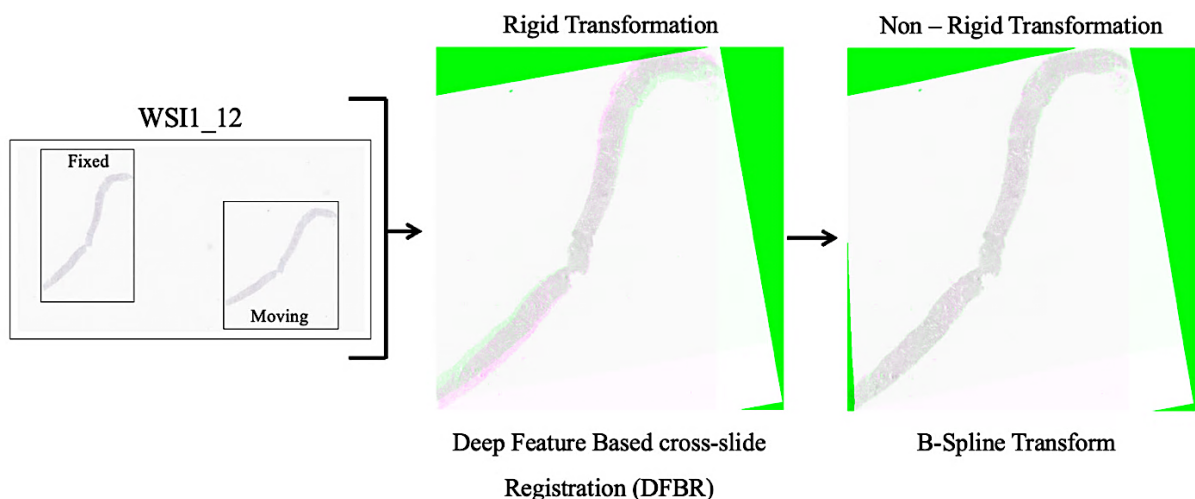
Figure 28 Image registration results for WSI1_12. On the left-hand side, the WSI includes selected fixed and moving images. Images are registered through both rigid transformations using DFBR (middle) and non-rigid transformations using B-spline transform (right side). The green section indicates the fixed image, and the pink section shows the registered image. Additionally, green borders denote the extra padding added to the moving image after registration to ensure the dimensions matched.[44]
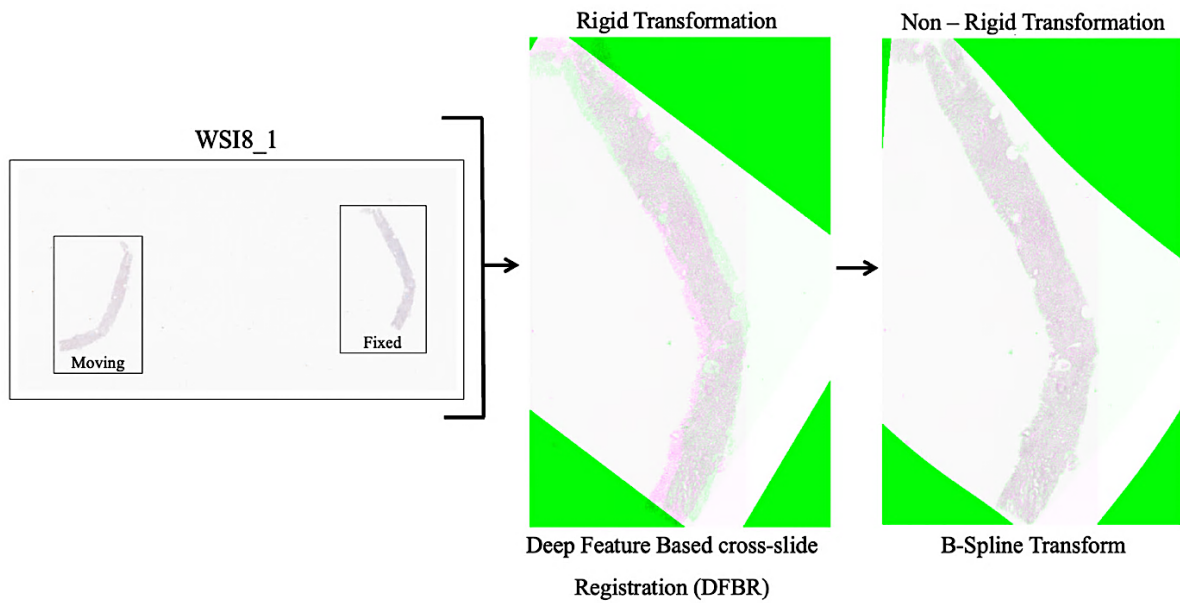
Figure 29 Image registration results for WSI8_1. On the left-hand side, the WSI includes selected fixed and moving images. Images are registered through both rigid transformations using DFBR (middle) and non-rigid transformations using B-spline transform (right side). The green section indicates the fixed image, and the pink section shows the registered image. Additionally, green borders denote the extra padding added to the moving image after registration to ensure the dimensions matched.[44]
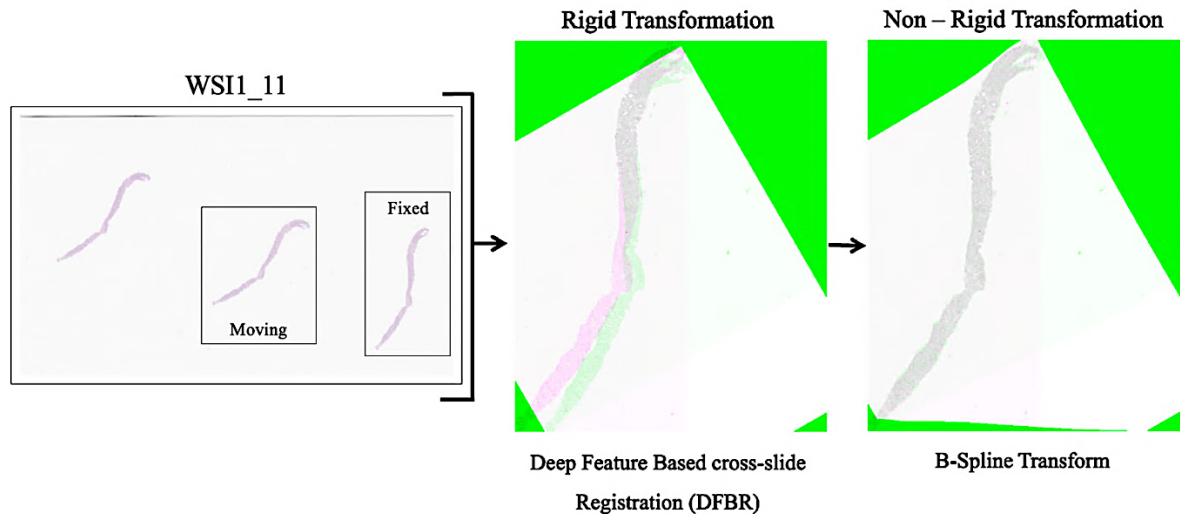

Figure 30 Image registration results for WSI4_1. On the left-hand side, the WSI includes selected fixed and moving images. Images are registered through both rigid transformations using DFBR (middle) and non-rigid transformations using B-spline transform (right side). The green section indicates the fixed image, and the pink section shows the registered image. Additionally, green borders denote the extra padding added to the moving image after registration to ensure the dimensions matched.[44]

4.2.3.2 Sections with Several Biopsy Cylinders

The registration results for WSIs containing biopsy cylinders were evaluated to test the pipeline's ability to handle diverse types of WSIs. Adjustments such as manually combining components, were made to the pre-processing pipeline to accommodate the unique characteristics of each WSI, ensuring accurate alignment and registration. For WSI2_1 (Figure 31), the pre-processing pipeline was adapted to identify six connected components, pairing them in sets of two for subsequent procedures. The registration process remained consistent, yielding IOU/DSC approximately 0.86/0.92. WSI6_1 (Figure 32) comprises three sections, each containing three compartments. During preprocessing, the three compartments within each section were combined and utilized for further registration, resulting in an IOU/DSC of 0.97/0.98. WSI10_1 (Figure 33) consists of two sections, each containing several compartments. However, parts of the cylinder on the right may not have been included in the fixed and moving images. During the detection of connected components, not all minor connected components were detected, so a decision was made to include only three compartments for each section in the further processing steps. The registration results yielded IOU/DSC of 0.90/0.95. WSI11_1 (Figure 34) comprised three sections, each featuring multiple compartments. The algorithm successfully detected entire sections by combining merely three connected components for both fixed and moving images. Following the standard registration procedure, the achieved results displayed an IOU/DSC of 0.68/0.81.

Figure 31 Image registration results for WSI2_1. On the left-hand side, the WSI includes selected fixed and moving images. Images are registered through both rigid transformations using DFBR (middle) and non-rigid transformations using B-spline transform (right side). The green section indicates the fixed image, and the pink section shows the registered image. Additionally, green borders denote the extra padding added to the moving image after registration to ensure the dimensions matched.[44]
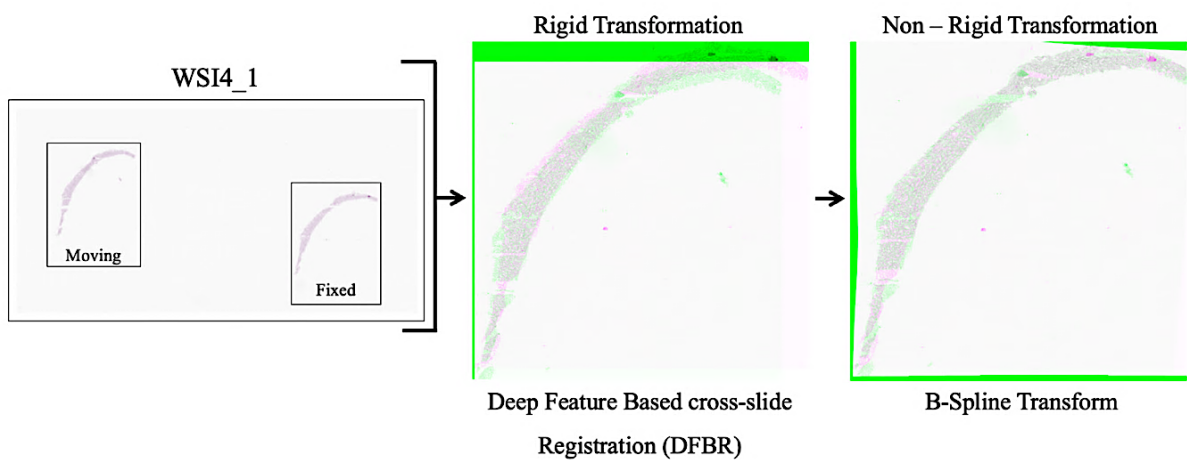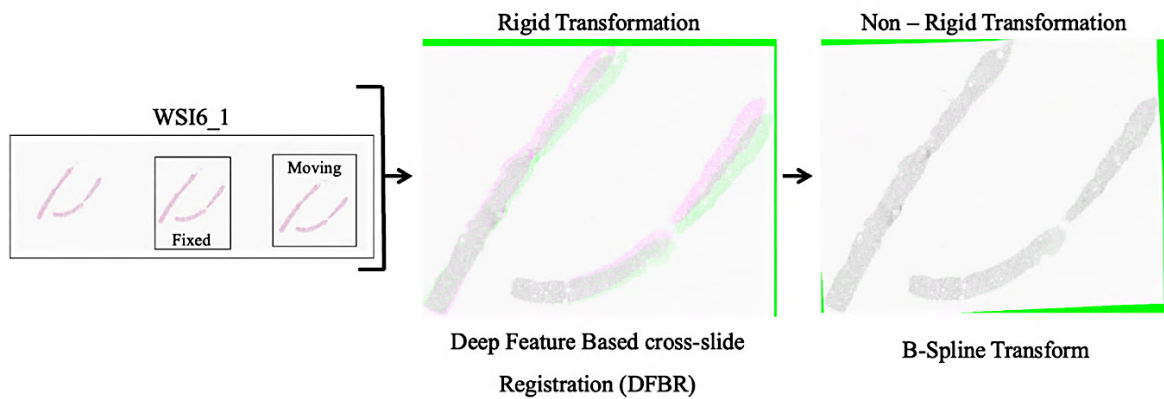
Figure 32 Image registration results for WSI6_1. On the left-hand side, the WSI includes selected fixed and moving images. Images are registered through both rigid transformations using DFBR (middle) and non-rigid transformations using B-spline transform (right side). The green section indicates the fixed image, and the pink section shows the registered image. Additionally, green borders denote the extra padding added to the moving image after registration to ensure the dimensions matched.[44]
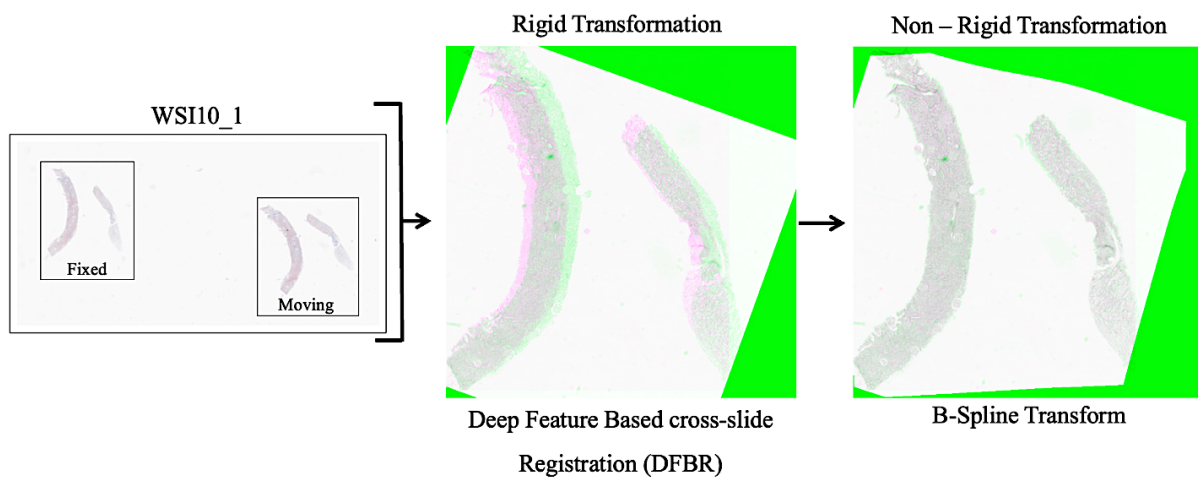
Figure 33 Image registration results for WSI10_1. On the left-hand side, the WSI includes selected fixed and moving images. Images are registered through both rigid transformations using DFBR (middle) and non-rigid transformations using B-spline transform (right side). The green section indicates the fixed image, and the pink section shows the registered image. Additionally, green borders denote the extra padding added to the moving image after registration to ensure the dimensions matched.[44]
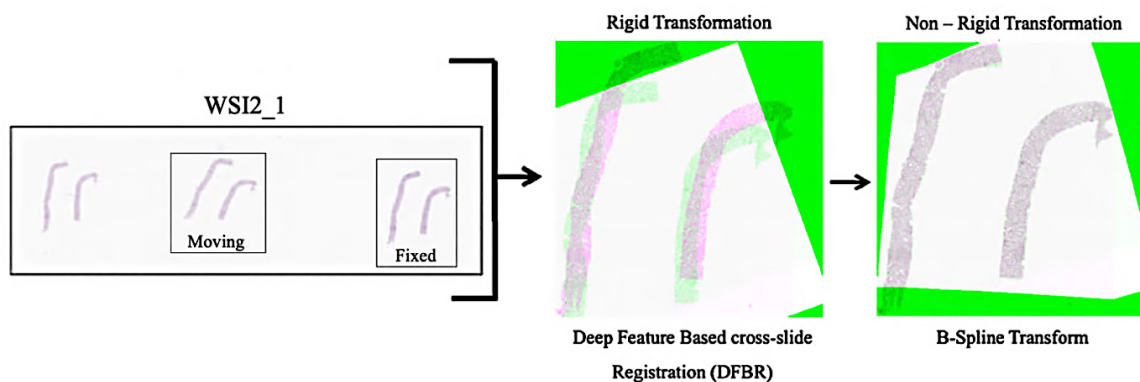
Figure 34 Image registration results for WSI11_1. On the left-hand side, the WSI includes selected fixed and moving images. Images are registered through both rigid transformations using DFBR (middle) and non-rigid transformations using B-spline transform (right side). The green section indicates the fixed image, and the pink section shows the registered image. Additionally, green borders denote the extra padding added to the moving image after registration to ensure the dimensions matched.[44]

4.2.3.3 Sections with More Complex Arrangements of Biopsy Cylinders

The registration results for WSIs with more complex arrangements of biopsy cylinders were evaluated to assess the pipeline's adaptability to intricate structures. Adjustments were made to the pre-processing pipeline, such as combining multiple components within each section, to handle the complexity and ensure accurate registration. For WSI3_1 (Figure 35), the pipeline combined four components from each section to form fixed and moving images, achieving an IOU/DSC of 0.95/0.97. WSI5_1 (Figure 36) involved combining four compartments within each section during preprocessing, resulting in an IOU/DSC of 0.89/0.94. WSI7_1 (Figure 37) comprised three sections, each with six compartments, which were combined for further registration, yielding an IOU/DSC of 0.94/0.97. For WSI9_1 (Figure 38) four compartments from each section were combined into a single compartment during preprocessing, leading to registration results of IOU/DSC 0.92/0.96. These results demonstrate the pipeline's capacity to manage and accurately register more complex biopsy cylinder arrangements.

Figure 35 Image registration results for WSI3_1. On the left-hand side, the WSI includes selected fixed and moving images. Images are registered through both rigid transformations using DFBR (middle) and non-rigid transformations using B-spline transform (right side). The green section indicates the fixed image, and the pink section shows the registered image. Additionally, green borders denote the extra padding added to the moving image after registration to ensure the dimensions matched.[44]
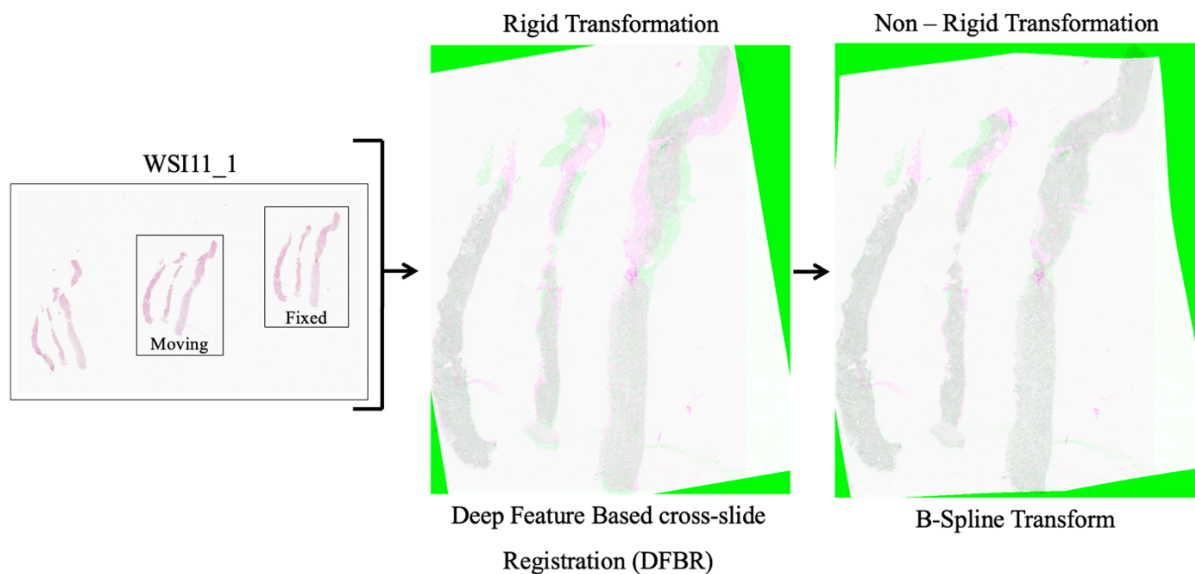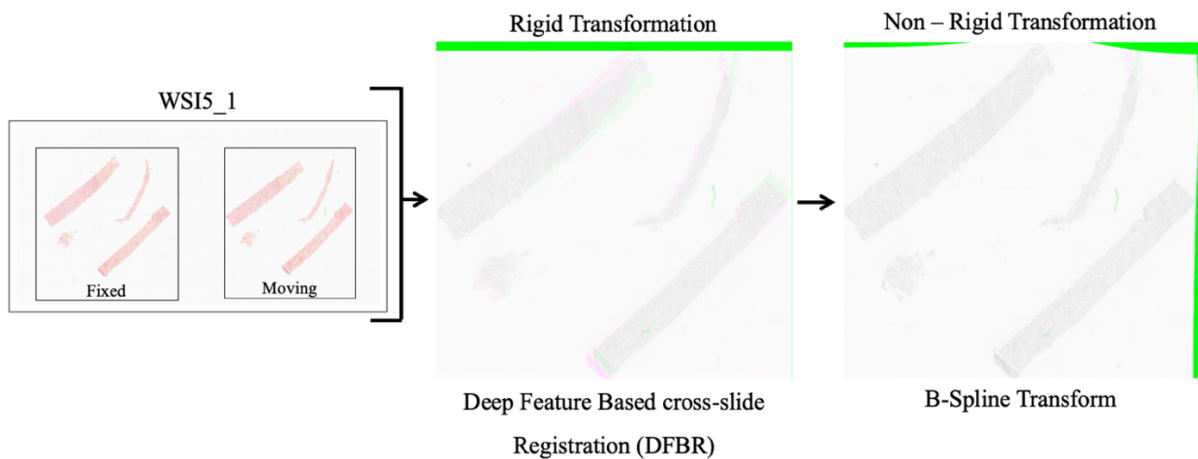

Figure 36 Image registration results for WSI5_1. On the left-hand side, the WSI includes selected fixed and moving images. Images are registered through both rigid transformations using DFBR (middle) and non-rigid transformations using B-spline transform (right side). The green section indicates the fixed image, and the pink section shows the registered image. Additionally, green borders denote the extra padding added to the moving image after registration to ensure the dimensions matched.[44]
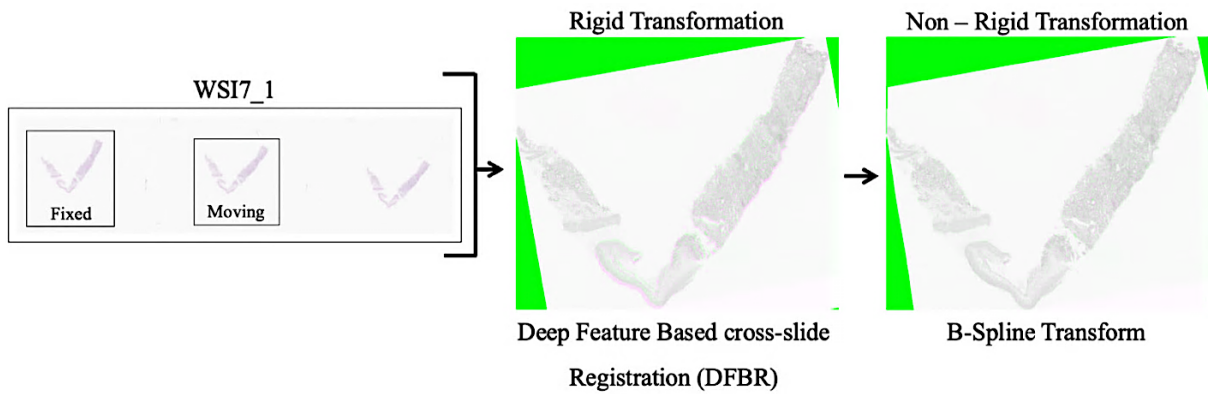
Figure 37 Image registration results for WSI7_1. On the left-hand side, the WSI includes selected fixed and moving images. Images are registered through both rigid transformations using DFBR (middle) and non-rigid transformations using B-spline transform (right side). The green section indicates the fixed image, and the pink section shows the registered image. Additionally, green borders denote the extra padding added to the moving image after registration to ensure the dimensions matched.[44]
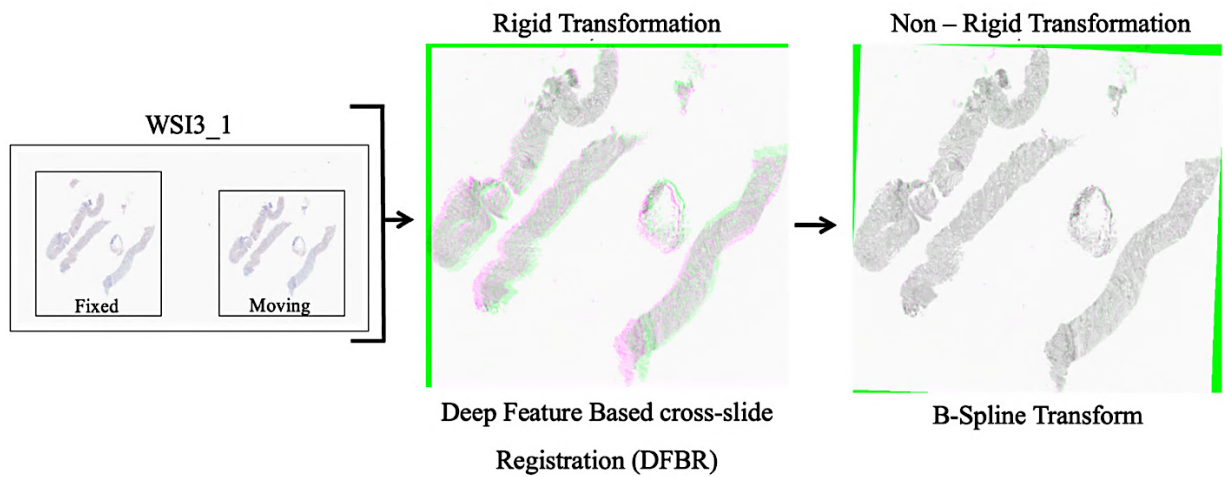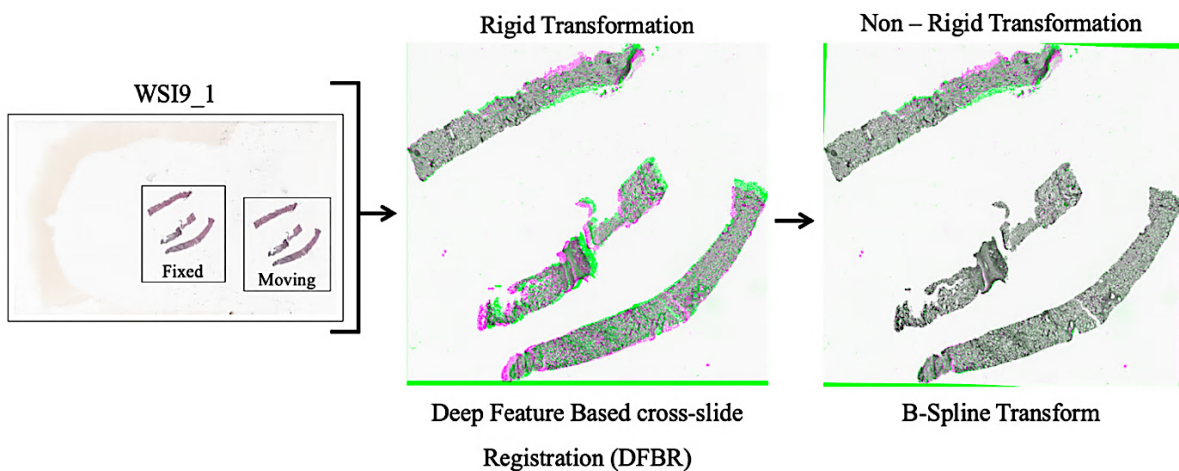

Figure 38 Image registration results for WSI9_1. On the left-hand side, the WSI includes selected fixed and moving images. Images are registered through both rigid transformations using DFBR (middle) and non-rigid transformations using B-spline transform (right side). The green section indicates the fixed image, and the pink section shows the registered image. Additionally, green borders denote the extra padding added to the moving image after registration to ensure the dimensions matched.[44]

4.2.3.4   Summary of Alignment Results for Diverse Cases

The evaluation of image registration performance was conducted on a variety of WSIs, each with unique structural characteristics. The results of these evaluations provide insight into the adaptability of the registration pipeline across different scenarios. Table 7 presents the alignment results in terms of IOU and DSC for each of the WSIs. The quality of the registration is assessed based on the complexity of the individual sections. Most WSIs demonstrated

favourable registration outcomes, with high IOU and DSC values. WSI4_1 and WSI11_1 achieved IOU/DSC values of 0.69/0.82 and 0.68/0.81, respectively. Although these values are slightly lower, they are still considered acceptable based on their structural complexity or damage. For instance, WSI4_1 have gaps in the tissue section, this is illustrated in figure 39. This indicates that while the majority of the WSIs showed satisfactory alignment performance, certain cases presented more challenging scenarios, yet still yielded reasonably satisfactory results.
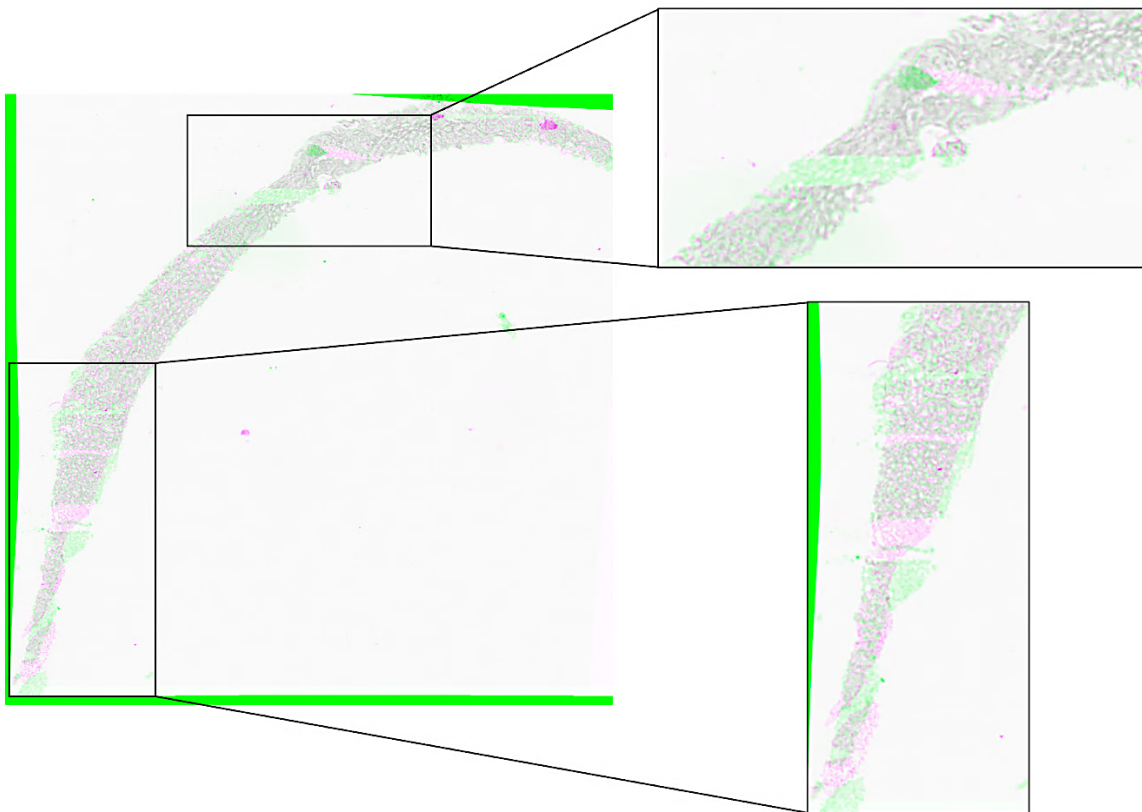
Figure 39 Non-rigids registration results of WSI4_1, illustrating gaps in the tissue section. On the left-hand side, non-rigid transformations using B-spline transform is presented. The green section indicates the fixed image, and the pink section shows the registered image. Additionally, green borders denote the extra padding added to the moving image after registration to ensure the dimensions matched.[44] The gaps in the tissue section (fixed and registered images) are illustrated in zoom-in view to the right.

53

Table 7 Alignment results for diverse cases.

Case no.	WSI	Downscaling Factor	IOU	DSC
Case 1	WSI1_6	40%	≈ 0.96	≈ 0.98
	WSI1_11	18x	≈ 0.93	≈ 0.96
	WSI1_12	18x	≈ 0.95	≈ 0.98
Case 2	WSI2_1	16x	≈ 0.86	≈ 0.92
Case 3	WSI3_1	18x	≈ 0.95	≈ 0.97
Case 4	WSI4_1	16x	≈ 0.69	≈ 0.82
Case 5	WSI5_1	18x	≈ 0.89	≈ 0.94
Case 6	WSI6_1	17x	≈ 0.97	≈ 0.98
Case 7	WSI7_1	17x	≈ 0.94	≈ 0.97
Case 8	WSI8_1	17x	≈ 0.91	≈ 0.95
Case 9	WSI9_1	17x	≈ 0.92	≈ 0.96
Case 10	WSI10_1	17x	≈ 0.90	≈ 0.95
Case 11	WSI11_1	17x	≈ 0.68	≈ 0.81

4.2.4 Application of TIAToolbox on Difficult Case

The pipeline underwent testing on three challenging cases: Difficult Case 1 (DC1), Difficult Case 2 (DC2), and Difficult Case 3 (DC3).

4.2.4.1 Error Encountered

While executing the image registration process using the DFBRegister model in TIAToolbox[44], a ValueError occurred in certain sections. All error presented in this section of the thesis refer to this ValueError. This error occurred while attempting to determine the optimal transformation for pre-alignment in difficult cases. Specifically, the issue arose during the estimation of the transform using tissue regions. The error message indicated a shape mismatch, although this had been addressed during the initial pre-processing steps, suggesting the presence of other underlying issues. Additionally, an error was encountered wherein the algorithm failed to identify the best transformation for pre-alignment. The error suggested to

54

try changing the values for 'dice_overlap', which is the dice ratio used for the selection of the best transformation matrix[44], and the 'rotation step', which is the increment in the rotation angles[44].

4.2.4.2 Difficult Case 1 (DC1)

In WSI_DC1 (Figure 38), unique challenges arose during registration testing. Two attempts were made to register Section 3 (fixed image) with both Section 2 and Section 1. The first attempt, using Section 2 as the moving image, yielded promising results with an IOU of approximately 0.72 and a DSC of around 0.84 (Figure 40 B). However, the registration algorithm failed in the second attempt with Section 1 as the moving image (Figure 40 A). As a workaround, the sections were divided into two parts for registration. The larger section achieved an IOU of about 0.88 and a DSC of around 0.94, indicating satisfactory registration. The smaller section was initially registered with the fixed image as a whole, but this attempt failed. Subsequently, the smaller section was registered with the corresponding smaller moving image, resulting in good performance with an IOU of approximately 0.84 and a DSC of about 0.91. These results suggest that the TIAToolbox registration algorithm requires similar positioning of sections for successful registration.
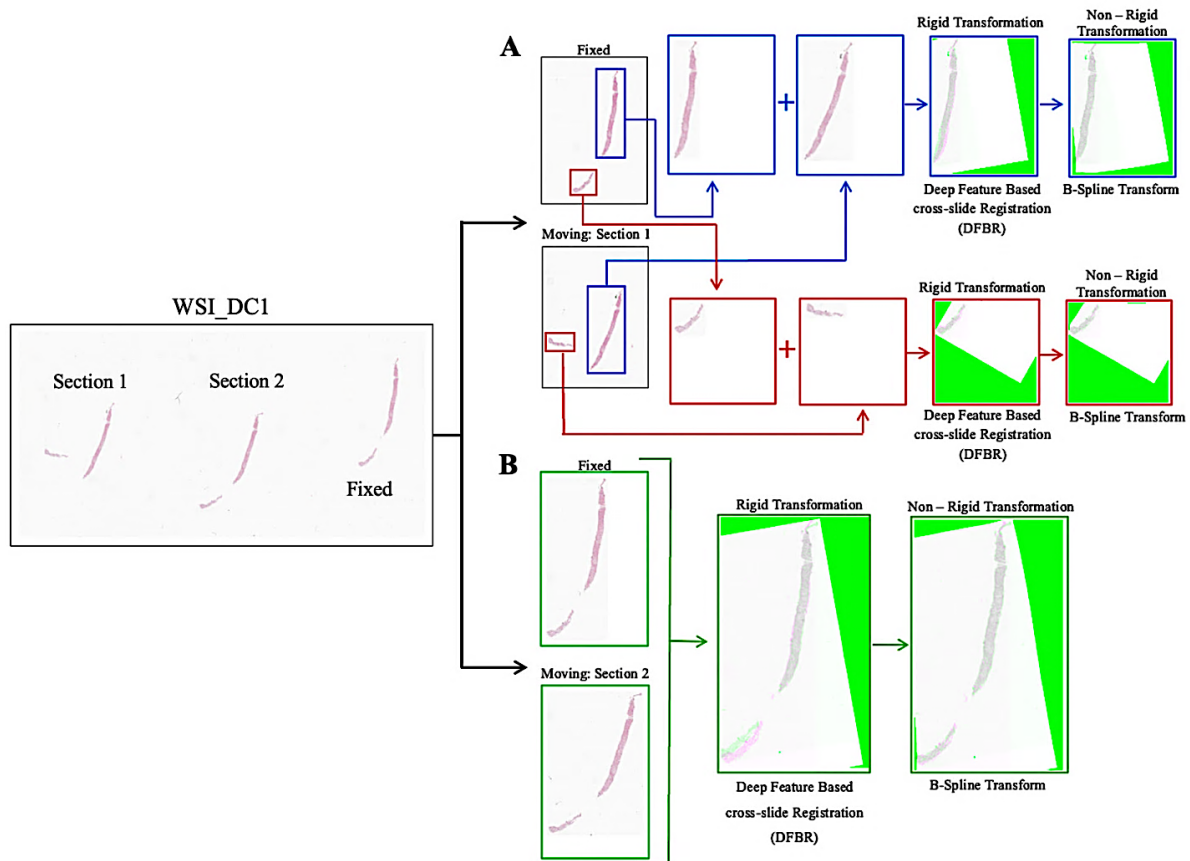
Figure 40 Registration attempts using DC1. In WSI_DC1, the fixed image (Section 3) was registered with both Section 1 and Section 2. A) Registration with Section 1 was unsuccessful, leading to its division into two parts for registration - smaller and larger components. The blue arrow and image border indicate the registration results for the larger sections, while the red arrow and image border indicate the registration of the smaller sections. B) The green arrows and image border represent registration with Section 2, demonstrating successful rigid and non-rigid transformations.

4.2.4.3 Difficult Case 2 (DC2)

In WSI_DC2, one of the two sections was damaged (Figure 41). The intact section served as the fixed image, while the damaged section was used as the moving image. However, the TIAToolbox registration algorithm encountered errors and failed to register these images. As an alternative approach, the sections were divided into three parts and registered individually. The registration attempt for the upper part was unsuccessful. In contrast, the registration for the second part, which was the largest component, was successful, resulting in an IOU of approximately 0.68 and a DSC of about 0.81. It's important to note that these metrics may not accurately reflect alignment due to the broken nature of the moving image, resulting in data loss. The lower part, representing the damaged section of the moving image, was also subjected to registration attempts. However, this process encountered errors as the algorithm failed to function properly.
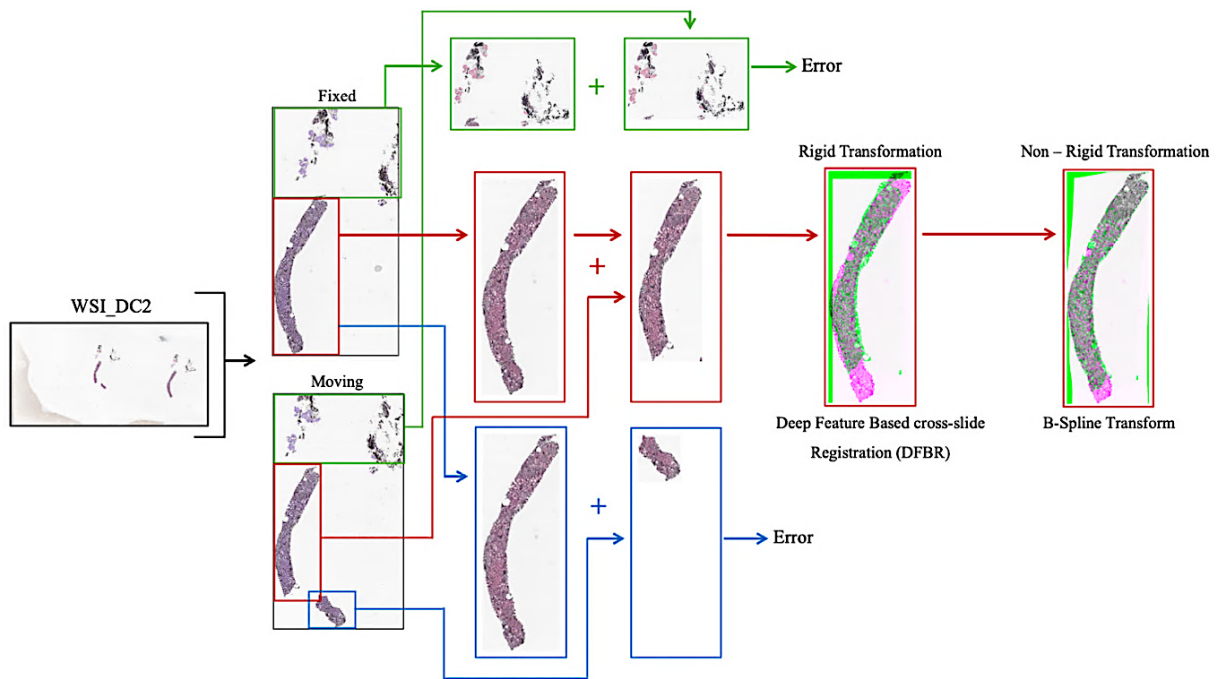
Figure 41 Registration attempts using DC2. In WSI_DC2, both the fixed and moving images were divided into three parts for alignment due to initial registration failure. The first part (green arrows and image borders) encountered error, while the second part (red arrows and image borders), comprising the largest components, achieved successful registration. However, the last part (blue arrows and image borders) also encountered error.

4.2.4.4 Difficult Case 3 (DC3)

In WSI_DC3 (Figure 42), the sections comprised two components: one small and one large. The small components aligned well using the TIAToolbox algorithm, achieving an IOU of approximately 0.93 and a DSC of around 0.96. However, aligning the larger components posed challenges. The fixed image was selected as the normal-looking section, while the moving image represented a section that had become folded during histological processing.

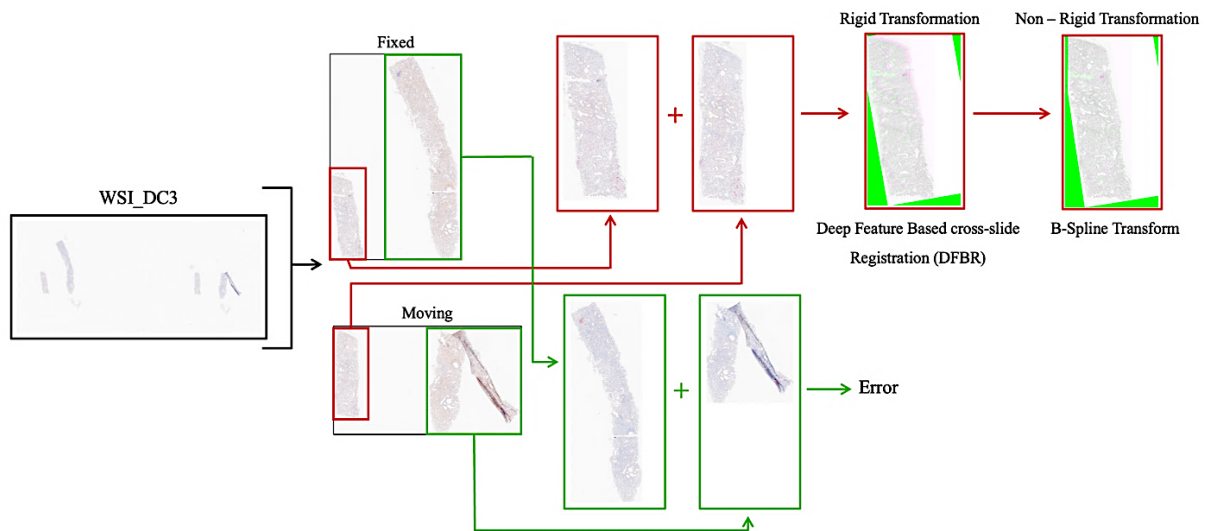**Figure 42 Registration attempts using DC3.** In WSI_DC3, the sections were divided into two parts, comprising small and large components. While the small components (red arrows and image borders) achieved successful registration, the large components (green arrows and image borders) did not achieve successful registration.

58

5 Discussion

The primary objective of this project was to investigate image registration tools for potential integration into a future pipeline designed to automate the alignment and ordering of non-neoplastic kidney biopsy sections. This study focused on evaluating the performance of image registration tools using non-neoplastic kidney biopsy WSIs obtained from the Renal Biopsy Laboratorium, Dept. of Pathology, Haukeland University Hospital, Bergen. By employing IOU and DSC metrics, the goal was to assess the effectiveness of HistokatFusion[43] (commercial) and TIAToolbox[44] (open source) image registration tools in this specific domain and to gain insights that could enhance the quality of image registration within a larger future pipeline.

In digital pathology, two widely discussed challenges in image registration are the large-scale nature of WSIs and the need for registration methods capable of handling deformations during histological processing. To address the former challenge, the approach involved downscaling images, reducing their resolution to make computational processing more manageable while retaining essential features for accurate registration. However, if the system configuration includes sufficient computational resources, downscaling may not be necessary for both the pre-processing and the registration process in both HistokatFusion and TIAToolbox. The latter challenge is typically tackled through the application of non-rigid transformations. TIAToolbox uses non-rigid transformation using B-spline transform[44] and HistokatFusion uses a dense non-linear approach[41, 46] which can adjust for deformations that occur during the preparation of histological samples.

5.1 Comparison with Existing Literature

Several studies provide valuable insights into the optimization of image registration in histopathology. Lotz et al.'s study emphasizes the importance of deformable registration methods by comparing consecutive and restained sections[38]. Lotz et al. also discuss limitations such as the reliance on landmarks for accuracy measurement and the need for comprehensive evaluation metrics. This thesis work utilized two tools employing non-rigid transformations. TIAToolbox uses B-spline transform[44], while HistokatFusion employs a dense non-linear

59

approach[41, 46]. However, this study relied on binary mask pixel-based evaluation rather than landmark-based evaluation, which represents a limitation.

Awan et al., focus on the registration of multiple sections within a tissue block, which is crucial for cross-slide image analysis[36]. Their research primarily employs DFBR, a rigid registration method, achieving precise alignment with minimal errors. This thesis uses the pre-alignment DFBR method by TIAToolbox, which is an advantage because it allows for better non-rigid registration.

No literature was found on the registration of sections from non-neoplastic kidney biopsy WSIs, which highlights the novelty of this study. Borovec et al.[41] mention using human kidney sections for registration with various tools, but certain pre-processing issues and challenges were not addressed.

5.2 Evaluating Methodology

5.2.1 Part I – Literature Review

To find image registration tools, a literature review was conducted. The literature review undertaken for this study was conducted aiming to encompass a wide range of relevant publications in the field of image registration applied to histological images. However, it is acknowledged that despite the thoroughness of the review process, there may be publications that were inadvertently missed. This could be attributed to the limitations of the search phrases used or the possibility of papers employing image registration techniques on histological images without explicitly mentioning terms such as "digital pathology" or "whole slide images." Therefore, while efforts were made to capture a broad spectrum of literature, there remains the potential for overlooked studies that may offer valuable insights into the topic at hand.

5.2.2 Image Pre-Processing

The pre-processing pipeline initially employed down-sampling of images to reduce computational complexity while preserving essential features required for accurate registration.

However, down-sampling may result in some loss of information, especially at the microscopic level. Nevertheless, the primary objective of this study was to evaluate the efficacy of image registration using TIAToolbox, with the intention of integrating it into a larger pipeline in the future. Given the importance of preserving microscopic details in the larger pipeline, down-sampling will not be included to avoid any potential loss of information.

During the pre-processing steps, manual input was necessary, such as specifying the number of connected components and manually combining separated components. Since the pipeline relies on connected components instead of manually cropping sections, there is a possibility that parts of the section might be mistakenly omitted. Additionally, adjustments were made to ensure uniform size and to address challenges such as the presence of small components within sections.

The current pre-processing pipeline remain partially automated due to manual inputs required. To automatically specify the number of connected components in histology images, several strategies can be considered. One approach involves testing numerous WSIs to establish a threshold size for detecting connected components. However, this method has a limitation which is that artifacts may sometimes exceed the size of broken sections, leading to potential misidentification by the algorithm. Another approach is instructing the algorithm to identify specific components that occur multiple times in a single WSI. A limitation to approach may be that certain WSIs may only contain one single section. However, in cases where artifacts are larger than the sections the algorithm could be trained to recognize specific morphological structures that are similar to a section as artifacts usually have a distinct shape. To overcome these challenges, one method that may work would be to integrate both strategies into the pipeline.

To automatically combine broken sections, or sections with several cylinders, one approach would be to detect instances where masks of sections appear repeatedly and pair different masks of sections when they occur multiple times within the image. For WSIs containing a single section, a size threshold could be applied to identify and combine the sections. Additionally, as mentioned earlier, the algorithm could be trained to recognize certain morphological structures to further refine the exclusion of artifacts. However, a challenge inherent to these approaches is the diversity among WSIs, which necessitates a large training dataset to enable the algorithm to accurately identify a wide range of patterns.

5.2.3 Rigid and Non – Rigid Registration

TIAToolbox employs the DFBR method for initial alignment, integrating fixed and moving images to achieve rigid transformation. Subsequently, non-rigid registration is performed using the B-Spline Transform algorithm, with adjustments to grid spacing and sampling percentage giving precise alignment. To further enhance non-rigid registration, several parameters could have been test, such as the dice overlap and the rotation step[44].

The advantage of the TIAToolbox algorithm is that it includes pre-processing steps that greyscale the images and as an output plots one image into green-channel and other in blue + red channel. The greyscaling may ensure that variations in stains may not affect the registration to a larger extent, however this is unsure as some images may lead to variations in the grey color. A limitation of this study is that stain variations have not been tested, and therefore a reference to support this understanding of the algorithm could not be included.

5.2.4 Intersection Over Union (IOU) and Dice Score (DSC)

To objectively compare the performance of the open-source TIAToolbox with the commercial HistokatFusion tool, a statistical analysis was conducted using IOU and DSC. These metrics provide a quantifiable means to evaluate the accuracy of image registration. The analysis began with the generation of fixed and registered binary masks for both tools. By determining the coordinates of the white pixels in these masks, the intersection and union of the pixel coordinates were calculated. These calculations enabled the precise computation of IOU and DSC values.

While the use of IOU and DSC as evaluation metrics ensures a rigorous and unbiased comparison, a limitation is that these metrics are based on binary masks rather than anatomical landmarks. This reliance on masks means the evaluation may not fully capture the accuracy of the registration at a detailed structural level. In figure 41, representing the difficult case 2 registration of the larger sections, it is observed that the non-rigid transformation output appears to drag the moving image to fit the fixed image, indicating inaccurate structural alignment. However, this discrepancy is not fully captured by the mask of the registered image. For a more comprehensive assessment, incorporating landmark-based evaluation methods

could provide additional insights into the precise alignment of corresponding anatomical features between images. In image registration, landmarks are points that are located in the same areas across two or more images[47]. One landmark-based evaluation method presented by Lotz, et al.[52] could involve evaluating the average and median of the median relative target registration error over all image pairs[46, 48].

5.3 Discussing Results

5.3.1 Comparison Between HistokatFusion and TIAToolBox

Two image registration tools evaluated in this study were HistokatFusion and TIAToolbox. The registration of WSI_6, down sampled by 40% and scaled additionally by 10x, was evaluated using IOU and DSC metrics. HistokatFusion achieved higher scores compared to TIAToolbox. Despite showing a slightly lower performance, TIAToolbox was chosen for further testing due to its open-source nature and potential for optimization and integration into larger pipeline. A limitation of this comparison is that only a single WSI (WSI_6) was used for evaluation, which may not provide a comprehensive assessment of the tools' performance across different types if WSIs and could lead to biased results.

5.3.2 Testing of Various Grid Space and Sampling Percent Values

Testing various grid spacings and sampling percentages revealed that higher grid spacings (200, 100, and 50) paired with higher sampling percentages yielded better IOU and DSC results compared to a grid spacing of 20. Additionally, higher grid spacings with lower sampling percentages resulted in reduced computational time. Among the tested parameter values, the best registration was obtained with a grid spacing of 200 and a sampling percentage of 1.0, providing a balance between alignment quality and computational efficiency.

An observation was made regarding poorer registration results with the lowest grid spacing (20 mm) despite a high sampling percentage. This suggests that an excessive number of control points can introduce noise, making it difficult for the algorithm to focus on the most important features. For instance, if the grid spacing decreases, the number of control points increases, causing the algorithm to struggle with aligning features at a microscopic level. The presence

of cells in one image but not in the other can further disrupt the alignment process, creating noise and potentially reducing the size of the moving image, as shown in figure 26B. Therefore, choosing the correct parameters is essential.

As mentioned, a grid spacing of 20 may be considered the lower boundary for good registration results. However, the upper boundary has not been identified, as grid spacings from 200 to 50 yielded nearly equivalent registration. Higher grid spacings should be tested to determine if they also provide good results. Additionally, computational time decreases as grid spacing increases, suggesting that higher grid spacings might be more suitable for higher-resolution images. A limitation of the conducted experiment is that only a single WSI was evaluated, so the identified lower and upper boundaries may not be generalizable to a wide range of WSIs.

5.3.3 Application of TIAToolbox on Diverse Sections

The evaluation of the pipeline across different WSIs, each with unique structural characteristics, underscores its adaptability. Most WSIs demonstrated satisfactory alignment performance, exceptions such as WSI4_1 and WSI11_1, which had lower IOU values, still yielded reasonably acceptable results. These outcomes highlight the pipeline's general efficacy while also pointing to specific cases that may require additional adjustments or refinements. Overall, these results indicate that while the pipeline performs effectively across various scenarios, continuous optimization and testing are important for handling the full spectrum of WSI variations encountered in practice.

5.3.4 Application of TIAToolbox on Difficult Cases

The evaluation of the pipeline on three challenging cases – Difficult Case 1 (DC1), Difficult Case 2 (DC2), and Difficult Case 3 (DC3) – highlights the algorithm's capabilities and limitations.

5.3.4.1 Error Encountered

To address the ValueError encountered during image registration process using DFBRegister model in TIAToolbox[44], several steps can be taken. First, ensure that pre-processing steps are accurately applied to the images. Then, adjust the 'dice_overlap' and 'rotation_step' values as suggested by the error message. If these attempts fail, consider preprocessing the images to ensure compatibility with TIAToolbox's registration process, or explore alternative registration methods.

5.3.4.2 Difficult Case 1

In DC1, using Section 3 as the fixed image, the registration with Section 2 yielded promising results, suggesting initial success. However, the algorithm failed when Section 1 was used as the moving image, necessitating a workaround. By dividing the sections into smaller parts, satisfactory registration was achieved with the larger part and the smaller part. These results indicate that the TIAToolbox algorithm is sensitive to the relative positioning of sections and may require pre-processing adjustments to enhance registration accuracy.

5.3.4.3 Difficult Case 2

In DC2, the broken nature of one section posed significant challenges. The intact section served as the fixed image, but the algorithm failed to register the damaged section effectively. Dividing the sections into smaller parts partially mitigated this issue. While the upper part could not be registered, the second part (the largest component) was able to be registered, however non-rigid registration output seemed to show that that moving image got dragged to fit the fixed image (Figure 41). This outcome highlights the inherent difficulty in registering damaged sections and underscores the importance of intact, well-preserved samples for reliable alignment. The failure to register the lower part further emphasizes the limitations when dealing with significant tissue damage.

5.3.4.4 Difficult Case 3

In DC3, the smaller components aligned well, demonstrating the algorithm's effectiveness with less complex structures. However, challenges arose with the larger components, particularly due to folding during histological processing. This indicates that while TIAToolbox performs

well with simpler, undamaged sections, more complex deformations like folding may present limitations for the registration algorithm. One potential approach to address this issue could be to substract the folded part from the fixed mask and use the new mask to register the lower part of the folded biopsy. For full automation, it would be advantageous to develop an algorithm capable of automatically detecting folds and artifacts that disrupt the registration process.

5.3.4.5 Alignment Challenges

The results from the challenging cases highlight key points about the pipeline's performance. Firstly, successful registration often depends on the relative positioning of sections, necessitating pre-processing steps such as realignment or splitting sections to enhance outcomes. Secondly, the algorithm struggles with broken sections, emphasizing the importance of for additional pre-processing to handle damaged tissues. Thirdly, complex deformations, such as folding or tearing during histological processing, present challenges; while smaller, simpler sections align well, larger or more damaged sections may require better techniques. Lastly, the variability in registration success across different WSIs suggest that further testing with a broader range of sections is necessary to identify specific scenarios where the pipeline excels and where it requires further refinement. The points underscore the robustness and flexibility of the pipeline while also highlighting areas for improvement in handling complex and damaged sections.

5.4 Areas for Improvement

To enhance the quality of the pre-processing and image registration pipeline, several areas for improvement have been identified. Firstly, a wider range of image registration tools beyond HistokatFusion and TIAToolbox must be evaluated to identify the most effective solutions. Additionally, various evaluation methods should be employed for a more comprehensive assessment, rather than relying solely on mask pixel-based methods such as IOU and DCS metrices. Secondly, during the evaluation process, multiple WSIs must be tested since WSIs can vary significantly from one another. Thirdly, once an effective tool, such as TIAToolbox, is identified, the pipeline should be tested on a broader range of WSIs to validate its performance across diverse samples. Additionally, several WSIs should be used when evaluating suitable grid spacing and sampling percentage values for TIAToolbox's non-rigid algorithm to ensure robust performance.

The pre-processing pipeline requires refinement to enable full automation. Initially, it should identify the optimal fixed image based on structural integrity across the sections of a whole slide image (WSI). Furthermore, the pipeline should automatically determine the number of connected components to include and which ones to combine. Additionally, to improve accuracy, the pipeline should possess the capability to detect artifacts such as folds and exclude them before initiating the registration process.

5.5 Further Research

Further research should be the development of methods to conduct image registration effectively, especially in challenging cases, and extend testing across diverse WSIs. Moreover, there is a need to advance the automatic preprocessing tool using the existing preprocessing pipeline. Additionally, it is imperative to design a pipeline for ordering non-neoplastic biopsy sections based on their cutting sequence during histological processing using a microtome. Integrating the preprocessing and image registration pipeline into this comprehensive framework will streamline the creation of a software tool capable of automatically aligning and ordering non-neoplastic kidney biopsy sections, thereby enhancing the efficiency of non-neoplastic kidney biopsy evaluation for nephropathologists.

5.6 Conclusion

In conclusion, this study evaluated a pre-processing pipeline for non-neoplastic kidney biopsy WSIs from Haukeland University Hospital, Bergen, along with the TIAToolbox image registration tool. The primary goal was to integrate these tools into a future pipeline for automating the alignment and ordering of biopsy sections. IOU and SDC metric were used to assess the effectiveness of both TIAToolbox and the commercial tool HistokatFusion.

Addressing challenges in digital pathology, the study found downscaling images can manage computational complexity, but sufficient resources may negate the need for downscaling. Non-rigid transformations were essential for handling histological deformations. TIAToolbox, despite slightly lower performance metrics than HistokatFusion, was chosen for its open-source potential and adaptability.

The evaluation showed that higher grid spacings and sampling percentages yielded better results. Most WSIs demonstrated satisfactory alignment, but challenging cases highlighted areas for improvement, such as handling damaged sections and complex deformations.

Further research and areas for improvement should focus on testing a wider range of WSIs, enhancing the automated pre-processing pipeline, and using alternative evaluation methods beyond IOU and DSC metric. These steps will improve the accuracy and efficiency of non-neo plastic kidney biopsy evaluations, benefiting nephropathologists and researchers.

Bibliography

1.   Kumar V, Abbas AK, Aster JC. Robbins Basic Pathology. 2017: Elsevier - OHCE. 10th ed. Available from: https://bookshelf.health.elsevier.com/books/9780323394147.
2.   Ekart R, Ferjuc A, Furman B, Gerjevič Š, Bevc S, Hojs R. Chronic kidney disease progression to end stage renal disease: a single center experience of the role of the underlying kidney disease. Ther Apher Dial. 2013;17(4):363-7. doi: 10.1111/1744-9987.12079. PubMed PMID: 23931872.
3.   Global, regional, and national burden of chronic kidney disease, 1990-2017: a systematic analysis for the Global Burden of Disease Study 2017. Lancet. 2020;395(10225):709-33. Epub 20200213. doi: 10.1016/s0140-6736(20)30045-3. PubMed PMID: 32061315; PMCID: PMC7049905.
4.   Vanholder R, Annemans L, Bello AK, Bikbov B, Gallego D, Gansevoort RT, Lameire N, Luyckx VA, Noruisiene E, Oostrom T, Wanner C, Wieringa F. Fighting the unbearable lightness of neglecting kidney health: the decade of the kidney. Clin Kidney J. 2021;14(7):1719-30. Epub 20210420. doi: 10.1093/ckj/sfab070. PubMed PMID: 34221379; PMCID: PMC8243275.
5.   Carriazo S, Villalvazo P, Ortiz A. More on the invisibility of chronic kidney disease… and counting. Clin Kidney J. 2022;15(3):388-92. Epub 20211127. doi: 10.1093/ckj/sfab240. PubMed PMID: 35198154; PMCID: PMC8690216.
6.   Kovesdy CP. Epidemiology of chronic kidney disease: an update 2022. Kidney Int Suppl (2011). 2022;12(1):7-11. Epub 20220318. doi: 10.1016/j.kisu.2021.11.003. PubMed PMID: 35529086; PMCID: PMC9073222.
7.   Aeffner F, Zarella MD, Buchbinder N, Bui MM, Goodman MR, Hartman DJ, Lujan GM, Molani MA, Parwani AV, Lillard K, Turner OC, Vemuri VNP, Yuil-Valdes AG, Bowman D. Introduction to Digital Image Analysis in Whole-slide Imaging: A White Paper from the Digital Pathology Association. J Pathol Inform. 2019;10:9. Epub 20190308. doi: 10.4103/jpi.jpi_82_18. PubMed PMID: 30984469; PMCID: PMC6437786.
8.   Gopalan C, Kirk E. Chapter 7 - Renal physiology. In: Gopalan C, Kirk E, editors. Biology of Cardiovascular and Metabolic Diseases: Academic Press; 2022. p. 123-40.
9.   Chen TK, Knicely DH, Grams ME. Chronic Kidney Disease Diagnosis and Management: A Review. Jama. 2019;322(13):1294-304. doi: 10.1001/jama.2019.14745. PubMed PMID: 31573641; PMCID: PMC7015670.
10.   Paolini. IVMMA. Histology, Kidney and Glomerulus: StatPearls 2023 [cited 2023 31/07]. Available from: https://www.ncbi.nlm.nih.gov/books/NBK554544/.
11.   Bülow RD, Boor P. Extracellular Matrix in Kidney Fibrosis: More Than Just a Scaffold. J Histochem Cytochem. 2019;67(9):643-61. Epub 20190522. doi: 10.1369/0022155419849388. PubMed PMID: 31116062; PMCID: PMC6713975.
12.   Lumen. Microscopic Anatomy of the Kidney: Module 9: The Urinary System [cited 2023 01/08]. Available from: https://courses.lumenlearning.com/suny-ap2/chapter/microscopic-anatomy-of-the-kidney/.
13.   NIH. Your Kidneys & How They Work: NIH: National Institue of Diabetes and Digestive and Kidney Diseases; [cited 2023 01/08]. Available from: https://www.niddk.nih.gov/health-information/kidney-disease/kidneys-how-they-work.
14.   Dalal R, Bruss ZS, Sehdev JS. Physiology, Renal Blood Flow and Filtration. StatPearls. Treasure Island (FL): StatPearls Publishing; 2024
.
15.   Rahman M, Siddik AB. Anatomy, Arterioles. StatPearls. Treasure Island (FL): StatPearls Publishing; 2024
.
16.   Barisoni L, Lafata KJ, Hewitt SM, Madabhushi A, Balis UGJ. Digital pathology and computational image analysis in nephropathology. Nat Rev Nephrol. 2020;16(11):669-85. Epub 20200826. doi: 10.1038/s41581-020-0321-6. PubMed PMID: 32848206; PMCID: PMC7447970.
17.   Aiforia. Overview of digital pathology and its benefits 2020 [cited 2024 16.05]. Available from: https://www.aiforia.com/blog/overview-of-digital-pathology.
18.   Niazi MKK, Parwani AV, Gurcan MN. Digital pathology and artificial intelligence. Lancet Oncol. 2019;20(5):e253-e61. doi: 10.1016/s1470-2045(19)30154-8. PubMed PMID: 31044723; PMCID: PMC8711251.

19.   Tizhoosh HR, Pantanowitz L. Artificial Intelligence and Digital Pathology: Challenges and Opportunities. J Pathol Inform. 2018;9:38. Epub 20181114. doi: 10.4103/jpi.jpi_53_18. PubMed PMID: 30607305; PMCID: PMC6289004.

20.   Jahn SW, Plass M, Moinfar F. Digital Pathology: Advantages, Limitations and Emerging Perspectives. J Clin Med. 2020;9(11). Epub 20201118. doi: 10.3390/jcm9113697. PubMed PMID: 33217963; PMCID: PMC7698715.

21.   Thorstenson S, Molin J, Lundström C. Implementation of large-scale routine diagnostics using whole slide imaging in Sweden: Digital pathology experiences 2006-2013. J Pathol Inform. 2014;5(1):14. Epub 20140328. doi: 10.4103/2153-3539.129452. PubMed PMID: 24843825; PMCID: PMC4023034.

22.   Vodovnik A. Distance reporting in digital pathology: A study on 950 cases. J Pathol Inform. 2015;6:18. Epub 20150430. doi: 10.4103/2153-3539.156168. PubMed PMID: 25969793; PMCID: PMC4421888.

23.   Stathonikos N, Nguyen TQ, Spoto CP, Verdaasdonk MAM, van Diest PJ. Being fully digital: perspective of a Dutch academic pathology laboratory. Histopathology. 2019;75(5):621-35. Epub 20190912. doi: 10.1111/his.13953. PubMed PMID: 31301690; PMCID: PMC6856836.

24.   Fraggetta F, Garozzo S, Zannoni GF, Pantanowitz L, Rossi ED. Routine Digital Pathology Workflow: The Catania Experience. J Pathol Inform. 2017;8:51. Epub 20171219. doi: 10.4103/jpi.jpi_58_17. PubMed PMID: 29416914; PMCID: PMC5760840.

25.   Retamero JA, Aneiros-Fernandez J, Del Moral RG. Complete Digital Pathology for Routine Histopathology Diagnosis in a Multicenter Hospital Network. Arch Pathol Lab Med. 2020;144(2):221-8. Epub 20190711. doi: 10.5858/arpa.2018-0541-OA. PubMed PMID: 31295015.

26.   Têtu B, Evans A. Canadian licensure for the use of digital pathology for routine diagnoses: one more step toward a new era of pathology practice without borders. Arch Pathol Lab Med. 2014;138(3):302-4. Epub 20130626. doi: 10.5858/arpa.2013-0289-ED. PubMed PMID: 23802851.

27.   L'Imperio V, Brambilla V, Cazzaniga G, Ferrario F, Nebuloni M, Pagni F. Digital pathology for the routine diagnosis of renal diseases: a standard model. J Nephrol. 2021;34(3):681-8. Epub 20200718. doi: 10.1007/s40620-020-00805-1. PubMed PMID: 32683656; PMCID: PMC8192318.

28.   Cazzaniga G, Rossi M, Eccher A, Girolami I, L'Imperio V, Van Nguyen H, Becker JU, Bueno García MG, Sbaraglia M, Dei Tos AP, Gambaro G, Pagni F. Time for a full digital approach in nephropathology: a systematic review of current artificial intelligence applications and future directions. J Nephrol. 2024;37(1):65-76. Epub 20230928. doi: 10.1007/s40620-023-01775-w. PubMed PMID: 37768550; PMCID: PMC10920416.

29.   Wilson PC, Messias N. How Whole Slide Imaging and Machine Learning Can Partner with Renal Pathology. Kidney360. 2022;3(3):413-5. Epub 20220211. doi: 10.34067/kid.0007982021. PubMed PMID: 35582192; PMCID: PMC9034807.

30.   Dawson H. Digital pathology - Rising to the challenge. Front Med (Lausanne). 2022;9:888896. Epub 20220722. doi: 10.3389/fmed.2022.888896. PubMed PMID: 35935788; PMCID: PMC9354827.

31.   Stathonikos N, Nguyen TQ, van Diest PJ. Rocky road to digital diagnostics: implementation issues and exhilarating experiences. J Clin Pathol. 2021;74(7):415-20. Epub 20200928. doi: 10.1136/jclinpath-2020-206715. PubMed PMID: 32988997.

32.   Besusparis J, Morkunas M, Laurinavicius A. A Spatially Guided Machine-Learning Method to Classify and Quantify Glomerular Patterns of Injury in Histology Images. J Imaging. 2023;9(10). Epub 20231011. doi: 10.3390/jimaging9100220. PubMed PMID: 37888327; PMCID: PMC10607091.

33.   Mola N, Hodneland E, Weishaupt H, Leh S, editors. Training a deep learning model for quantification of fibrosis in non-neoplastic kidney biopsies - a feasibility study
. 34th European Congress of Pathology; 2022; Switzerland, Congress Center Basel.

34.   O'Keeffe M, Oterhals Å, Weishaupt H, Leh S, Ulvik A, Ueland PM, Halstensen A, Marti HP, Gudbrandsen OA. A diet containing cod backbone proteins attenuated the development of mesangial sclerosis and tubular dysfunction in male obese BTBR ob/ob mice. Eur J Nutr. 2023;62(8):3227-40. Epub 20230807. doi: 10.1007/s00394-023-03227-4. PubMed PMID: 37550593; PMCID: PMC10611847.

35.   Lutnick B, Manthey D, Becker JU, Ginley B, Moos K, Zuckerman JE, Rodrigues L, Gallan AJ, Barisoni L, Alpers CE, Wang XX, Myakala K, Jones BA, Levi M, Kopp JB, Yoshida T, Zee J, Han SS, Jain S, Rosenberg AZ, Jen KY, Sarder P. A user-friendly tool for cloud-based whole slide image segmentation with examples from

renal histopathology. Commun Med (Lond). 2022;2:105. Epub 20220819. doi: 10.1038/s43856-022-00138-z. PubMed PMID: 35996627; PMCID: PMC9391340.

36.   Awan R, Raza SEA, Lotz J, Weiss N, Rajpoot N. Deep feature based cross-slide registration. Comput Med Imaging Graph. 2023;104:102162. Epub 20221219. doi: 10.1016/j.compmedimag.2022.102162. PubMed PMID: 36584537.

37.   Shackleford J, Kandasamy N, Sharp G. Chapter 2 - Unimodal B-Spline Registration. In: Shackleford J, Kandasamy N, Sharp G, editors. High Performance Deformable Image Registration Algorithms for Manycore Processors. Boston: Morgan Kaufmann; 2013. p. 13-43.

38.   Lotz J, Weiss N, van der Laak J, Heldmann S. Comparison of consecutive and restained sections for image registration in histopathology. J Med Imaging (Bellingham). 2023;10(6):067501. Epub 20231130. doi: 10.1117/1.Jmi.10.6.067501. PubMed PMID: 38074626; PMCID: PMC10704256.

39.   Marstal K, Berendsen F, Staring M, Klein S, editors. SimpleElastix: A User-Friendly, Multi-lingual Library for Medical Image Registration. 2016 IEEE Conference on Computer Vision and Pattern Recognition Workshops (CVPRW); 2016 26 June-1 July 2016.

40.   Klein S, Staring M, Murphy K, Viergever MA, Pluim JP. elastix: a toolbox for intensity-based medical image registration. IEEE Trans Med Imaging. 2010;29(1):196-205. Epub 20091117. doi: 10.1109/tmi.2009.2035616. PubMed PMID: 19923044.

41.   Borovec J, Kybic J, Arganda-Carreras I, Sorokin DV, Bueno G, Khvostikov AV, Bakas S, Chang EI, Heldmann S, Kartasalo K, Latonen L, Lotz J, Noga M, Pati S, Punithakumar K, Ruusuvuori P, Skalski A, Tahmasebi N, Valkonen M, Venet L, Wang Y, Weiss N, Wodzinski M, Xiang Y, Xu Y, Yan Y, Yushkevich P, Zhao S, Munoz-Barrutia A. ANHIR: Automatic Non-Rigid Histological Image Registration Challenge. IEEE Trans Med Imaging. 2020;39(10):3042-52. Epub 20200407. doi: 10.1109/tmi.2020.2986331. PubMed PMID: 32275587; PMCID: PMC7584382.

42.   OpenAI. ChatGPT 2023.

43.   Daniel Budelmann, Johannes Lotz, Nick Weiss. HistokatFusion Lübeck: Fraunhofer MEVIS; 2021 [cited 2024]. Available from: https://histoapp.pages.fraunhofer.de/about/.

44.   Pocock J, Graham S, Vu QD, Jahanifar M, Deshpande S, Hadjigeorghiou G, Shephard A, Bashir RMS, Bilal M, Lu W, Epstein D, Minhas F, Rajpoot NM, Raza SEA. TIAToolbox as an end-to-end library for advanced tissue image analytics. Commun Med (Lond). 2022;2:120. Epub 20220924. doi: 10.1038/s43856-022-00186-5. PubMed PMID: 36168445; PMCID: PMC9509319.

45.   DataCamp. Preprocessing and Filtering Techniques in Signal Processing: Handling noise and outliers 2024 [cited 2024]. Available from: https://www.datacamp.com/tutorial/a-data-scientists-guide-to-signal-processing#.

46.   Lotz J, Weiss N, Heldmann S. Robust, fast and accurate: a 3-step method for automatic histological image registration. CoRR. 2019;abs/1903.12063. Epub Sat, 23 Jan 2021 01:19:43 +0100.

47.   CustusX. Tutorial: Image Landmark Registration 2023 [cited 2024]. Available from: https://www.custusx.org/uploads/user_doc/nightly/tutorial_image_landmark_registration.html#:~:text=Image%20landmark%20registration%20is%20a,moving%20in%20the%20registration%20process.

48.   Borovec J, Munoz-Barrutia A, Kybic J, editors. Benchmarking of Image Registration Methods for Differently Stained Histological Slides. 2018 25th IEEE International Conference on Image Processing (ICIP); 2018 7-10 Oct. 2018.